Article:

Jin, J, Wang, X, Zhang, Z et al. (8 more authors) (2022) Shallow gas and gas hydrate accumulations influenced by magmatic complexes in the Pearl River Mouth Basin, South China Sea. Marine Geology, 453. 106928. ISSN 0025-3227

https://doi.org/10.1016/j.margeo.2022.106928

Shallow gas and gas hydrate accumulations influenced by magmatic complexes in the Pearl River Mouth Basin, South China Sea

Jiapeng Jin[a,b], Xiujuan Wang[a,b]*, Zhengyi Zhang[c,b], Min He[d], Craig Magee[e], Jie Li[d], Yuanping Li[d], Sanzhong Li [a,b], Zhendong Luan[c,b], Guangxu Zhang[c,b], Luyi Sun[c,b]

[a] *Frontiers Science Center for Deep Ocean Multispheres and Earth System, Key Lab of Submarine Geosciences and Prospecting Techniques, MOE and College of Marine Geosciences, Ocean University of China, Qingdao 266100, China*

[b] *Laboratory for Marine Mineral Resources & Deep-sea Multidisciplinary Research Center，Pilot National Laboratory for Marine Science and Technology (Qingdao)，Qingdao 266237, China*

[c] *Center for Ocean Mega-Science, CAS Key Laboratory of Marine Geology and Environment & Center of Deep-Sea Research, Institute of Oceanology, Chinese Academy of Sciences, Qingdao 266071, China*

[d] *Shenzhen Branch of China National Offshore Oil Corporation Ltd, Shenzhen, 518054, China*

[e] *Institute of Geophysics and Tectonics, School of Earth and Environment, University of Leeds, Leeds, LS2 9JT, UK*

Abstract

We analyse occurrences of gas hydrates and free gases above a 1200 km^2 complex of igneous volcanoes and sills using newly acquired three-dimensional (3D) seismic data in the Pearl River Mouth Basin of the South China Sea. In strata above volcano summits, we recognize three enhanced reflection layers at different stratigraphic levels, including discontinuous Bottom Simulating Reflectors (BSRs) and pluming BSRs. We also show that the lateral tips of eight sills, which at times appear to terminate against supra-sill faults, underlie gas chimneys linked to gas hydrate and free gas in shallower strata. These supra-sill faults and gas chimneys, as well as supra-volcano faults, provided pathways for upward fluid (gas) migration from deep sources. Given the spatial relationship between volcanoes, sills, free gas, and gas hydrates, we suggest that the igneous structures focused fluid migration into overlying faults and gas chimneys. We also explore whether higher geothermal gradient at the summits of the volcanoes caused the base of gas hydrate stability zone to be shallower, forming a pluming BSR. Our study highlights how volcanic systems can influence the formation and distribution of later gas hydrate and free gas.

Keywords: Gas hydrate; Free gas; Magmatism; Fluid migration; Pearl River Mouth Basin

1. **Introduction**

Gas hydrates are crystalline solids that can form in low-temperature and high-pressure conditions, and are found often within sedimentary basins along continental margins, in permafrost, and potentially under ice sheets (Shipley et al., 1979; Sloan and Koh, 2007; Hornbach et al., 2008). The generation of highly saturated gas hydrate is controlled by the availability of hydrocarbon gas released from a source and the presence of migration pathways that enable gas to flow to a suitable reservoir where it can become trapped (e.g., Collett et al., 2009). However, as the temperature and/or pressure of such reservoirs changes, any present gas hydrates may destabilize and disaggregate, causing gas to migrate into surrounding strata (e.g., Hornbach et al., 2008; Collett et al., 2009). The evolution of hydrate-bearing reservoir temperature and/or pressure conditions may thus affect gas energy supply, seafloor failure, ocean acidification, and the global redistribution of carbon (e.g., Biastoch et al., 2011; Rupple and Kesler, 2017; Wu et al., 2022).

In addition to containing gas hydrates, many sedimentary basins across the continental margins contain evidence of significant magmatic events, some of which were associated with the release of substantial volumes of hydrocarbon and carbon dioxide-rich hydrothermal fluids (e.g., Planke et al., 2005; Jamtveit et al., 2004; Svensen et al., 2006; Grove, 2013; Omosanya et al., 2018; Phillips and Magee, 2020). Such magmatism can also drive host rock deformation (e.g., compaction and uplift) and locally elevate temperatures (e.g., Schutter, 2003; Jamtveit et al., 2004; Sun et al., 2020b, 2022a). Magmatism can thus influence the structural, thermal, and geodynamic evolution of sedimentary basins and petroleum systems (e.g., Schutter, 2003; Planke et al., 2005; Infante-Paez & Marfurt, 2017; Sun et al., 2020b, 2022a), and could therefore impact concurrent or later gas hydrate evolution. For example, in the Joetsu basin, Japan Sea, massive gas hydrates have been formed by a mixture gases related to magmatic-mantle fluids that migrated upwards through gas chimneys (Snyder et al., 2020). Gas hydrate and fluid migration pathways forming from carbon dioxide-rich fluids in the mid-Okinawa trough, Japan, have also been related to a magmatic source (Sakai et al., 1990; Hou et al., 2005).

In this study, we use reprocessed and newly acquired three dimensional (3D) seismic reflection data to explore potential links between sills, volcanoes, and gas hydrates. In particular, we examine how normal faults and gas chimneys connect gas-related enhanced reflections and BSRs to buried volcanoes and sub-volcanic sills in parts of the Pearl River Mouth Basin, South China Sea. The Pearl River Mouth Basin is a key exploration area for oil, gas, and gas hydrate in the South China Sea (e.g., Zhang et al., 2007; Pang et al., 2008; Yang et al., 2015, 2017). Gas hydrates and accompanying free gas have been confirmed in the area by logging while drilling (LWD) during the drilling expeditions GMGS1, 3, 4, and 5 (e.g., Zhang et al., 2007; Yang et al., 2015, 2017a). There is also evidence for intense, ancient magmatic activity within the Pearl River Mouth Basin (e.g., Zhao et al., 2016, 2019; Kong et al., 2018), which appears to have influenced fluid migration pathways (Sun et al., 2019, 2020b, c, d). We explore the age of magmatic activity in our study area and how volcanic systems potentially influence the formation of fluid migration pathways.

2. Geological Setting

2.1 Regional geology

The South China Sea developed through multiple phases of continental rifting between 75-40 Ma (Tg-T80) and 40-32 Ma (T80-T70), and records a rift-to-drift transition (Hayes and Nissen, 2005; Ding et al., 2018, 2020). Rifting was controlled by subduction of the Palaeo-Pacific Plate below the Eurasian Plate (Deng et al., 2019; Ding et al., 2019, 2020; Wang et al., 2021). The Pearl River Mouth Basin is located on the northern slope of the South China Sea (Fig. 1a) and its formation involved a syn-rift stage in the Eocene (~75 Ma to 32 Ma), a phase of continental breakup in the Oligocene (32 Ma to 23.8 Ma), and a final post-rift subsidence stage since the Miocene (23.8 Ma to recent) (Fig. 2; e.g., Clift and Lin, 2001; Pang et al., 2008). Three main tectonic events have since affected the evolution of the Pearl Mouth River Basin, including the Zhuqiong Event (~23.8 Ma), the Baiyun Event (23.8–10.5 Ma), and the Dongsha Event (beginning at 10.5 Ma, and peaking at 5.5 Ma) (Lüdmann and

Wong, 1999; Zhao et al., 2016, 2019; Sun et al., 2020c, d). Magmatic activity in the Pearl River Mouth Basin mainly occurred in two stages at 64-32 Ma and 23.8-15.5 Ma (e.g., Yan et al., 2006; Li et al., 2014; Zhao et al., 2016, 2019; Sun et al., 2019, 2020b, c, d; Zeng et al., 2019; Zhang et al., 2021).

The study area is specifically situated in the Baiyun Sag, which comprises numerous submarine canyons on the continental slope, and the Yunli Low Uplift (Fig. 1). The Yunli Low Uplift separates the Baiyun Sag from the Liwan Sag, and hosts a volcano exposed on the present day seafloor (Fig. 1b, the white dashed line). Deep-water gas-fields (e.g., LW3-1-1), as well as a gas hydrate occurrence zone, occur within the Baiyan Sag (Fig. 1).

2.2 Stratigraphy and petroleum system

Continental, lacustrine facies mudstones and coals in the Late Cretaceous-Early Oligocene Wenchang and Enping formations represent the regional hydrocarbon source rocks in the Baiyun Sag, supplying sufficient thermogenic gas for gas fields and free gas accumulations (Fig. 2; e.g., Pang et al., 2008; Zhu et al., 2009). Marginal marine sandstones were deposited during the Late Oligocene-Early Miocene (Zhuhai and Zhujiang formations), which form the most important hydrocarbon reservoirs and carrier beds in the Baiyun Sag (Fig. 2; Zhu et al., 2009). Above these, deep-water depositional systems of the Hanjiang, Yuehai and Wanshan formations developed, as well as bathyal-abyssal mudstones and silty mudstones deposited in the submarine canyon-ridge system on the continental slope of Pearl River Mouth Basin (e.g., Zhou et al., 2015). The Dongsha event (10.5 Ma to present) induced limited regional uplift, erosion, and faulting within the Pearl River Mouth Basin (e.g., Su et al., 1989; Zeng et al., 2019), inducing the release of overpressured fluid in the Baiyun Sag (Kong et al., 2018); it has been suggested that this overpressure release provided the hydrocarbon gas required for development of the concentrated gas hydrates found in the area (Wang et al., 2011; Sun et al., 2020a).

2.3 Magmatic complexes (VCI, VCII and VCIII) in the Baiyun Sag

Recent studies have shown post-rift magmatism was widely distributed in the northern South China Sea (e.g., Zhao et al., 2016, 2019; Song et al., 2017; Yang et al., 2017b; Wang et al., 2019b; Zeng et al., 2019; Sun et al., 2020b, c, 2022a; Zhang et al., 2021), producing magmatic complexes in the west (VCI) and centre (VCII) of the Baiyun Sag (Fig. 3). Drilling of the VCI and VCII reveals the volcanoes comprise hydrothermally altered basalt lavas and tuffs, intercalated with thin-bedded limestone and clastic beds (Li and Rao, 1994; Zhao et al., 2016; Sun et al., 2020c). Igneous activity at VCI occurred between the start of the Miocene (23.8 Ma) and the end of the Early Miocene (17.6 Ma), as suggested by the K-Ar dating and seismic-stratigraphic relationships (Qin et al., 2000; Sun et al., 2014; Zhao et al., 2016). Many submarine volcanic mounds, associated lava flows, and underlying igneous sills are associated with VCI; they can be identified by their high amplitude and positive polarity reflections in seismic data (Sun et al., 2014; Zhao et al., 2016, 2019; Ma et al., 2018). Shallow gas accumulations with negative-polarity reflections are commonly located directly above volcanoes and linked to them by normal faults (Sun et al., 2014; Zhao et al., 2016; Yang et al., 2017b).

In this study, we focus on the VCIII magmatic complex, which spans the southeastern Baiyun Sag (referred to as the Shenhu area) and the Yunli Low Uplift (Figs. 3 and 4). Previous studies have recognized from seismic reflection data that a large seamount dominates the center of VCIII (Fig. 1b, the white broken line; Zhou et al., 2018; Zhao et al., 2019; Sun et al., 2022b), but its architecture and relationship with the hydrocarbon and gas hydrate system is poorly known.

2.4 Geological controls on gas hydrate occurrence

In the Shenhu gas hydrate-drilling area, high-amplitude reflections just above bottom-simulating reflectors (BSRs) have been interpreted as accumulations of gas hydrate with elevated saturations (e.g., Yang et al., 2015, 2017a; Wang et al., 2016, 2021). These BSRs primarily occur along the crest of four ridges (Wang et al., 2014, 2016; Yang et al., 2015, 2017a; Zhang et al., 2017, 2020; Qian et al., 2018; Jin et al., 2020a). High concentrations of gas hydrate accompanying free gas and structure II gas hydrate (i.e. composed of heavy-hydrocarbon gases) have been confirmed at borehole sites W18, W19, W11 and W17 (Fig. 1A) (e.g., Yang et al., 2015, 2017a; Qian et al., 2018; Wei et al., 2018); quantitative modelling indicates that gas hydrates formed ~29,000-19,000 years ago at Sites W18 and W19 (Fang et al., 2019; Jin et al., 2020a). The gas compositions in the core samples at Sites W18, W19 and W17 are mainly composed of methane (C1), heavy hydrocarbon gases (C2), and a small amount of carbon dioxide (CO_2, 100-300 ppm) (Zhang et al., 2007; Yang et al., 2015, 2017a; Qian et al., 2018). Double BSRs or II-BGHSZ (base of gas hydrate stability zone) have been found due to the influence of thermogenic gas and complex sedimentation and erosion of the migrating canyons (e.g., Qian et al., 2018; Zhang et al., 2020a). Overall, localized high-temperature and mixed hydrocarbon gases (thermogenic and biogenic gases) are likely responsible for the occurrence of the recent active hydrate system and structure II gas hydrate in the Baiyun Sag (Jin et al., 2020a; Sun et al., 2020a). Normal faults and gas chimneys appear to have provided the pathways for fluid migration from deeper sedimentary thermogenic and biogenic gas sources (e.g., Wu et al., 2009; Wang et al., 2011; Zhang et al., 2017, 2020a, b; Cheng et al., 2020; Jin et al., 2020a).

3. Data and Methods

3.1 Seismic data and interpretations

We use high-resolution, 3D seismic reflection data of the Yunli Low Uplift that were acquired and processed by the China National Offshore Oil Corporation (CNOOC) in 2018. The 3D seismic data in the study area covers ~1300 km^2 (Fig. 1). Acquisition involved 390 channel streamers and 6 cables >4950 m in length. The bin spacings are 12.5 m and 25 m in the in-line and cross-line directions, respectively, and the sampling interval is 2 ms. The dominant frequency gradually decreases downward from the seafloor (~50 Hz) to where the igneous features of interest are located (~35 Hz). Using P-wave velocities of 1.5 km/s to 2.7 km/s for the interval of interest strata and 4.5 km/s for the volcanic complexes, determined from the Site BY7-1-1 borehole by Sun et al., (2020d), we calculate that the vertical seismic resolution ($\lambda/4$) decreases from ~7.5 m at the seafloor to ~20 m in the sedimentary strata hosting the volcanic complexes. Seismic attributes, such as variance, maximum and minimum amplitudes, and root mean square (RMS) were extracted from the 3D seismic data to help reveal discontinuous structures and the distributions of gas hydrate and free gas in the Baiyun Sag and Yunli Low Uplift.

We mapped horizons corresponding to prominent, positive polarity reflections marking the top of volcanoes (TM). In addition to a positive polarity, we defined sills based on their high-amplitude reflections and lateral discontinuity (Planke et al., 2005). Eleven regional strata sequence boundaries were mapped and tied to the nomenclature proposed by CNOOC (Figs. 2 and 3), specifically: Seafloor, T20 (2.49 Ma), T30 (5.5 Ma), T32 (10.5 Ma), T35 (13.5 Ma), T40 (15.5 Ma), T50 (17.5 Ma), T60 (23.8 Ma), T70 (32.0 Ma), T80 (40 Ma), Tg (65 Ma) (e.g., Pang et al., 2008; Dong et al., 2009; Ma et al., 2018). The ages of strata reflections onlapped onto volcanoes were used to constrain the relative time of igneous activity (Trude et al., 2003; Planke et al., 2005, 2017).

3.2 BSR classifications

In the seismic data, bottom simulating reflectors (BSRs) are interpreted to be the result of a negative impedance caused by the transition from gas hydrate-bearing and water-bearing sediments above to free gas-bearing sediments below, and approximately represent the base of gas hydrate stability zone (BGHSZ) (e.g., Shedd et al., 2012; Wang et al., 2014). Three types of BSR can be identified in the seismic profiles, namely continuous BSRs, discontinuous BSRs and pluming BSRs. The continuous and discontinuous BSRs have been identified in previous studies as they cross-cut strata, are marked by a polarity reversal, and are subparallel the seafloor

(Wang et al., 2016; Zhang et al., 2020a). We refer to pluming BSRs as areas where a BSR is locally elevated and shows an approximate convex toward the seafloor shape, perhaps indicative of a shallower BGHSZ related to the presence of hot fluids (Holbrook et al., 1996; Shedd et al., 2012; Daigle and Dugan, 2014; Le et al., 2015).

High amplitude and positive polarity reflections above the BSR(s) have been interpreted as gas hydrate in seismic profiles in the area (Wang et al., 2016). Similarly, polarity reversals and enhanced reflections associated with underlying velocity pull-down reflections below the BSR(s) have been interpreted as free gas and gas migration pathways (e.g., Collett et al., 2009; Boswell et al., 2012; Yoo et al., 2013).

3.3 Calculating the base of gas hydrate stability zone (BGHSZ)

The BGHSZ marks the bottom boundary where gas hydrate is stable and its position is controlled by the temperature, pressure conditions, pore water salinity, and gas compositions of the near-seabed sediments (Xu and Ruppel, 1999; Sloan and Koh, 2007). In general, gas hydrate occurs above this basal boundary and hydrocarbon gas (mainly methane) is trapped below the BGHSZ. Mostly, the depth of BGHSZ corresponds to the BSR found from the seismic data in the Pearl River Mouth Basin (e.g., Wang et al., 2014; Qian et al., 2018; Jin et al., 2020a). Due to a lack of well log data in the Yunli Low Uplift, we simulated the BGHSZ to help identify the boundary between gas hydrate and free gas. Specifically, parameters of inferred seafloor temperature, geothermal gradient from Sites SH2, SH3 and SH5 (Zhang et al., 2007) were used to calculate the likely depth of the BGHSZ for methane using the CSMHYD program (Sloan and Koh, 2007). The modelled depths of the BGHSZ were changed into time domain using an average velocity for the near-seabed sediment of is 1650 m/s, which was obtained from Site W25 (Zhou et al., 2022). We added the modelled and time-converted BGHSZ as a horizon within the seismic reflection data and compared its location to the interpreted BSRs and pluming BSRs. Based on the modelled location of the BGHSZ, we extracted coincident maximum, average positive, and minimum amplitude attributes from the seismic reflection data to show the distributions of gas hydrate and free gas. Mmaximum and average positive amplitude attributes are widely used to display the distribution of hydrates as they highlight positive waveforms related to gas hydrate above the BGHSZ (e.g. Wang et al., 2016; Portnov et al., 2021). In contrast, the minimum amplitude attribute extracted below the BGHSZ shows negative waveform information indicating the distribution of free gas (e.g. Wang et al., 2016).

4. Results

4.1. Gas accumulations

Seismically anomalous responses of free gas characterized by low frequency, negative polarity, laterally restricted, and enhanced reflections have been widely identified in the study area. In the gas hydrate-drilling area of Baiyun Sag, the minimum amplitude attribute extracted along the modelled BGHSZ within the four submarine canyons of the Baiyun Sag shows that enhanced reflection zones along both the ridges and the troughs (Fig. 5a, b). The enhanced reflections occur as either isolated seismic features distributed along a discrete stratigraphic level, or are marked by stacked reflection pairs that span several stratigraphic layers below the BGHSZ (Figs. 6 and 7). Gas trapped below the BSRs (or BGHSZ) but above T35 (15.5 Ma) is underlain by faults and/or ‘chimneys’ where background seismic reflections are locally dim and disturbed (Figs. 6a, b and 7).

In the Yunli Low Uplift, south of the gas hydrate-drilling zone, the distributions of enhanced reflections occur broadly in three zones to the north of the VCIII central volcanic edifice (Fig. 8a). These enhanced reflections are recognized above the summits of three buried volcanoes (M1, M2 and M3; see section 4.3) at three different stratigraphic levels (Fig. 9). The deepest enhanced reflection occurs above M1, ~600–650 ms two-way travel time (TWT) below the seafloor and coincides with T32 (10.5 Ma) (Fig. 9a, e). The second deepest layer broadly occurs along T30 (5.5 Ma) above M2 and can reach up to the BGHSZ where it develops into a discontinuous or pluming BSR, ~250–330 ms TWT below the seafloor (Fig. 9b, e). The shallowest enhanced reflection occurs above M3, ~180-200 ms TWT below the seafloor and just beneath T20 (2.49 Ma), and is locally marked by a pluming BSR (Fig. 9c, d, e).

4.2. Gas hydrate occurrence

4.2.1 Gas hydrate in the Baiyun sag

The modelled BGHSZ, which partly coincides with the BSRs, occurs ~250–300 ms TWT below the seafloor on the seismic sections (Figs. 6 and 7). We extract the maximum amplitude and average positive amplitude attribute along the BGHSZ with a time window that extends 50 ms TWT upward to show the distribution of gas hydrate-bearing layers (Fig. 5c, d). In plan-view, there is a NW-SE linear but patchy distribution of high amplitude with positive polarity reflectivity along the four crests of submarine ridges in the Baiyun Sag (Fig. 5c, d). The continuous BSRs occur at Sites SH2 and W17 (Figs. 6a, b, c and 7), while a discontinuous BSR is developed at Site W18 (Fig. 6d and 7a). In places, instances of single or multiple high amplitude reflections occur above the BSR (Figs. 6 and 7); these have been confirmed as corresponding to gas hydrates by drilling (e.g., Zhang et al., 2007; Yang et al., 2015, 2017a).

4.2.2 Gas hydrate in the Yunli Low Uplift

In the Yunli Low Uplift, potential gas hydrate-bearing layers are revealed by the maximum amplitude attribute map and occur along a broad zone that terminate north of the VCIII (Fig. 8b). Discontinuous BSRs and pluming BSRs are observed in shallow sediments above the M2 and M3 volcanoes (Fig. 9e-f). The discontinuous BSR is developed in shallow sediments (325 ms TWT below the seafloor) to the north of M2, above three or four small volcanoes (Fig. 9b). Similar discontinuous, moderate-high amplitude, layer reflections occur in this area above the BSR, perhaps indicating the potential local occurrence of gas hydrate-bearing sediments (Fig. 9b). Pluming BSRs occur above the summits of the M2 and M3 volcanoes; these Pluming BSRs comprise high-amplitude, convex-upwards reflections that cross-cut background stratigraphic reflections and are shallower than the modelled BGHSZ (Fig. 9b, c, the blue broken line). The pluming BSR is shallower above M3 (189 ms TWT below seafloor) than that above M2 (245 ms TWT below seafloor). Localized high amplitude reflections above the pluming BSRs potentially indicate the occurrence of gas hydrates (Fig. 9d).

4.3. Volcanoes

All identified volcanoes have a common top surface (TM), which is typically characterized by a high-amplitude, positive polarity reflection (Fig. 9). We recognize a large central volcanic edifice (VCIII) in the Yunli Low Uplift, which has a ~15 km diameter, is ~1100 ms TWT high (~2640 m assuming an interval velocity of 4.8 km/s), breaches the seafloor, and is surrounded by a series of buried, smaller volcanoes with diameters <1 km (Fig. 4). Of these smaller volcanoes, we focus on those we name M1, M2 and M3 as they appear to underlie free gas, gas hydrate, and BSR features in shallower strata (Fig. 9). M1 has a diameter of ~2 km, a height of ~250 ms TWT (~290 m), and its summit is situated ~900 ms TWT (~1000 m) below the seafloor (Fig. 9a). M2 comprises two summits situated ~700 ms TWT (~800 m) below the seafloor, and has a diameter of ~2.5 km and a height of ~400 ms TWT (~460 m) (Fig. 9b). M3 is closest (~4 km) to the large central volcano, has a summit ~500 ms (~570 m) below the seafloor, a diameter of ~2 km, and a height of ~270 ms (~310 m) (Fig. 9c). The oldest horizon that onlaps onto the volcanoes is T40 (15.5 Ma) (Fig. 9a, b). Above the volcanoes in places, strata display minor convex-upward folds and associated normal faults that offset the fold crests (Fig. 9).

4.4. Sills

Positive polarity, laterally discontinuous, and moderate-to-high amplitude reflections that are either concordant with or cross-cut surrounding reflections are observed between T80 and T50 (Fig. 6b). We interpret these as igneous sills, and eight sills were found in this area, named S1-8. The geometries of three types of sills are recognized: sub-horizontal, inclined, and saucer-shaped (Fig. 6e-h). Eight sills were mapped, mainly located within the Baiyun Sag in the northern margin away from the large central volcano. These sills have widths ranging from 0.7-8 km and lengths of 2-13 km (Figs. 6 and 7). Many normal faults appear to intersect the edges of sills in the deeper strata, and connect upwards to the shallow free gas and gas hydrate-bearing sedimentary rocks (Figs. 6 and 7c). Sills recognized within the volcanoes are poorly imaged and difficult to map clearly.

4.5. Faults and gas chimneys

Normal faults and gas chimneys are widely developed. A variance slice extracted near T32 shows a few E-W striking tectonic faults, which occur between T20 (2.49 Ma) and Tg (Figs. 3 and 10). Normal faults also occur above the sills across the gas hydrate-drilling area and these strike NW-SE (Fig. 10); these supra-sill faults extend down deepest from T80 (40 Ma) and commonly intersect lateral sill tips, but poor imaging often hinders their recognition at deeper levels (Figs. 6 and 7). Supra-sill faults are usually ~1000-3000 ms TWT and 6-8 km in length (Figs. 6b, 7c and 10); these are taller than those faults found above volcanoes, which are developed between T40 (16.5 Ma) and T20 (2.6 Ma), and thus ~500 ms TWT (<600 m) high (Fig. 9a, b, c). Supra-volcano faults have lengths of <3 km in the Yunli Low Uplift (Fig. 10), and are often radially distributed (Fig. 11a-c).

Features interpreted as gas chimneys are characterized by acoustic blanking, chaotic reflections, and/or velocity pull-downs and are the most common in the gas hydrate drilling area (e.g., Wu et al., 2009; Sun et al., 2012; Wang et al., 2014; Cheng et al., 2021). These chimneys occur above the sills and volcanoes and are 200-3500 ms TWT (230-4100 m) high (Figs. 6, 7 and 9). For example, in the Yunli Low Uplift, gas chimneys occur within folded strata above volcano summits (Fig. 9). Variance slices show gas chimneys have high variance values and, if isolated, are sub-circular in plan-view at horizon T32 (Fig. 10). Most of the gas chimneys are linearly distributed along the crest of four submarine canyons (Fig. 10).

4.6. Summary of spatial correlation between gas accumulations and igneous features

We overlaid maps to show the relationships between the various geological elements we identify and the occurrences of free gas and potential gas hydrate (Fig. 12). The supra-sill faults are developed within the potential gas hydrate and free gas zones of the Baiyun Sag and appear to connect the sills with shallow enhanced-reflections and high-amplitude layers (Figs. 6 and 7). For example, the continuous BSR appear connected to sill S8, which occurs at ~6.5 s TWT (~7.5 km), by three normal faults at Site SH2 (Fig. 6a, b). Similarly, normal faults appear to connect multiple layers of enhanced reflections to sills S5 and S7 near Sites W11 and W17 (Fig. 7c). In the Yunli Low Uplift, free gas- or potential hydrate-bearing layers occur above the summit of buried volcanoes M1, M2, and M3 (Figs. 10 and 12). There is no obvious gas hydrate distribution at the top of M1, as the free gas-bearing layer is much deeper than the modelled BGHSZ (Figs. 9a, e and 12a). Both supra-volcanic faults and gas chimneys occur above the summit of M2 and M3, and appear to connect the volcanoes to the shallower potential gas hydrate- and free gas-bearing sediments (Figs. 9, 10, and 12).

5. Discussion

5.1 Age of magmatism and associated structures

The central volcanic edifice (VCIII) and surrounding volcanoes (e.g., M1-M3) occur at the same stratigraphic level and are onlapped by T40, implying they extruded just before ~15.5 Ma. The age of VCIII is thus similar to VCI and VCII in the Baiyun Sag. In the west of the Baiyun Sag, VCI is 17.1±2.5Ma (Early Miocene), and the oldest volcanic material intersected by BY7-1-1 yields a K-Ar date of 35.5±2.78 Ma (Middle Eocene) (Qin, 2000). In the centre of the Baiyun Sag, seismic-stratigraphic onlap relationships suggest the volcanic plumbing system of VCII was mainly emplaced after 17.5 Ma, with activity ceasing before 15.5 Ma (Zhao et al., 2016, 2019).

There is no borehole data from the sills and no clear seismic-stratigraphic relationships (e.g., onlap onto intrusion-induced forced folds) that we can use to constrain their age of emplacement (e.g., Trude et al., 2003). However, the sills occur within strata between ~T80-T50, suggesting some if not all were therefore emplaced after 23.8 Ma (Figs. 6 and 10). Due to their close spatial association with the volcanoes, we suggest that the sills were likely emplaced at the same time as and fed volcanism (Sun et al., 2022b).

Sedimentary layers directly above the volcanoes (such as M1) show a four-way dip closures, i.e. dome-shaped folds (Fig. 9a, c). These folds occur in strata deposited long-after after the volcanoes were formed (~15.5 Ma) and are thus not related to magmatism; e.g., T32 (10.5 Ma) is often folded within these structures, indicating the folds formed over ~5 Myrs after volcanism. The shallowest folded strata observed is probably the horizon T30 (i.e. 5.5 Ma) (Fig. 9b). We suggest fold formation was likely due to differential compaction, whereby the igneous material comprising the volcanoes compacted less than the adjacent sedimentary column meaning strata directly above the volcanoes does not subside as much as elsewhere (e.g., Phillips and Magee, 2020; Wang et al., 2022). Associated with this differential compaction folding was the development of crestal normal faults and probably micro-fractures in response to outer-arc stretching (e.g., Cosgrove and Hillier, 1999).

5.2 Gas migration and gas hydrate accumulation influenced by magmatic activity

Fluid migration from deeply buried sedimentary rocks along the faults, gas chimneys, and permeable inclined strata have been widely reported in many basins to influence gas hydrate accumulation and distribution (e.g., Kinoshita et al., 2011; Boswell et al., 2012; Collett et al., 2019; Saito et al., 2019; Cheng et al., 2020; Portnov et al., 2020, 2021). In the Gulf of Mexico, for example, the location of gas hydrate reservoirs is often governed by salt diapirism, which causes overlying anticlinal structures favorable for accumulation of gas and gas hydrate, and an associated fault array that provides potential fluid flow pathways (Boswell et al., 2012; Portnov et al., 2020). Several studies have also found that intrusive and extrusive magmatic features can focus syn- and post-emplacement fluid migration in sedimentary basins, such as offshore southeastern Australia (Holford et al., 2017), in the central Atlantic magmatic province (Capriolo et al., 2021), and in the Møre basin of the northeast Atlantic continental (Svensen et al., 2004). In these works, it has been argued that emplacement and cooling fracture networks in igneous intrusions improve their permeability, such that when sills are interconnected (i.e. a sill-complex) they can provide extensive migration pathways (Rateau et al., 2013). Similarly, within volcanoes, the complex intercalation of lavas and volcaniclastics, which can have high porosities and permeabilities, and presence of igneous intrusions can facilitate fluid flow (Holford et al., 2017). However, as of yet there have been few studies examining the structural control magmatic systems play on gas hydrate occurrence.

In the Baiyun Sag, normal faults and gas chimneys extending upwards from different stratigraphic levels seem to provide important pathways for fluid migration, which has led to the formation of extensive free gas and gas hydrate (Figs. 6 and 7, e.g., Wu et al., 2009; Wang et al., 2011; Zhang et al., 2017; Cheng et al., 2020; Jin et al., 2020a). We show that some of the free gas accumulations are located directly above and vertically connected to volcanoes and sills by faults and gas chimneys, and are trapped in differential compaction folds above the volcanic complex (Fig. 9, Zhao et al., 2016; Ma et al., 2018; Sun et al., 2020b). These seismic-stratigraphic relationships indicate fluid migration and gas accumulation occurred long-after magmatism ceased, but that the intrusion network and volcanoes were porous and/or permeable enough that fluids exploited them as pathways. Upon reaching the lateral tips of sills or summits of volcanoes, these fluids then migrated along supra-sill and supra-volcano faults to shallower reservoirs and traps.

5.3 The thermodynamic influences on the BGHSZ

The pluming BSRs, characterized by localized, bright spots, discontinuous reflections (Fig. 9b, c), may be caused by locally elevated geothermal gradient compared to the surrounding area (Shedd et al., 2012), or diverse gas composition effects due to salt-driven evolution on gas hydrate system (Portnov et al., 2021). We just calculate the changes of BGHSZ by the influence of temperature due to lack of gas compositions in this area. By comparing the modelled BGHSZ to the observed BSR locations, the thermodynamic impact of volcanoes on the gas hydrate occurrence can be evaluated. We calculated the depth of the BGHSZ assuming the gas was pure methane, but used various geothermal gradients and seafloor temperatures to interpret the anomalous changes at three sites above M2 and M3 (Fig. 13a, b, c, locations 1-3 shown in Fig. 9b and c). Location 1 occurs above the volcanic basement, but not above a volcano, and is marked by a discontinuous BSR reflection at 325 ms TWT, which corresponds to a depth of 259 m using the P-wave velocity of 1650m/s at Site W25. Here, the modelled depth of the BGHSZ, comprising 100% methane, is 274 m using a seafloor temperature of 5.53 °C and a geothermal gradient of 49.31 °C/km (based on data from Site SH3), as well as a water depth of 1766 m (Fig. 13a); this makes the BGHSZ slightly deeper than the observed BSR depth. Both of Location 2 and Location 3 show pluming BSRs above M2 and M3 at depths of 245 ms and 189 ms TWT, which broadly equate to depths of 195 m and 159 m, respectively (Table 1). The modelled depths of the BGHSZ at locations 2 & 3 are 208 m and 204 m, given a high geothermal gradient of 67.60 °C/km and a seafloor temperature of 4.72 °C (based on data from Site SH5), as well as water depths of 1830 m and 1789 m (Fig. 13b, c and Table 1). The pluming BSRs above M2 and M3 occur at shallower levels than the BGHSZ modelled using the geothermal gradient measured at Site SH5. The calculated BGHSZ for thermogenic gas mixing will be deeper than that for pure methane, according to the hydrate phase equilibrium curve (Sloan and Koh, 2007). There may be an interplay between temperature and gas composition effects. For example, an increase in temperature would drive BSR formation upwards, whereas a gas mix containing heavier hydrocarbons would drive BSR formation downwards.

Similar to seafloor cold seeps that occur above the southern summit of the Hydrate Ridge, Cascadia subduction zone (e.g., Torres et al., 2004), the abnormally shallow BSRs we observe may be related to locally active hot fluids. Such anomalously shallow BSRs can also be formed due to overheating of seafloor sediments and the geothermal field not reaching equilibrium due to seafloor erosion (Bang et al., 2005; Jin et al., 2020b). However, we observe no evidence of seafloor erosion above or near the buried volcanoes (Fig. 9). Moreover, the spatial overlap between the pluming BSRs, free gas, and volcanoes (Fig. 12) suggests that the pluming BSRs could be influenced by upward flow of warm/hot fluids from the buried volcanoes. Salt bodies in the Gulf of Mexico have similarly been shown to focus warm/hot fluid flow, locally elevating the geothermal gradient (e.g., Portnov et al., 2020).

Table 1 Comparison of calculated BGHSZ and identified BSR depths at three locations.

BGHSZ	Water depth (m)	Geothermal gradients (℃ /km)	Seafloor temperature (℃)	Observed BSR in TWT (ms)	Observed BSR in depths (m)	Calculated BGHSZ (m)
Location 1	1766	49.31	5.53	325	259	274
Location 2	1830	67.60	4.72	245	195	208
Location 3	1789	67.60	4.72	189	159	204

5.4 Controlling factors on the free gas and gas hydrate accumulation

Gas hydrate drilling expeditions indicate that the migration of deep thermogenic and biogenic gas from the Wenchang and Enping formations (i.e. below T70) and shallow formations (i.e. T40 to present) in the Baiyan Sag occurred between 14-6.5 Ma and 5-0 Ma, after igneous activity at ~17.5-15.5 Ma (e.g., Yang et al., 2015, 2017a; Zhao et al., 2016; Qian et al., 2018; Su et al., 2018; Sun et al., 2020a, c, d; Zhang et al., 2020b). A small amount of CO_2 (100-300 ppm) was found in the gas hydrate-bearing samples at Sites W18, W19 and W17 (Zhang et al., 2007, 2020a), which may be related with volcanic-sourced fluids, similar to those found in the Japan Sea (Snyder et al., 2020). Alternatively, the CO_2 may be sourced from microbial degradation of petroleum (i.e. organic matter) (e.g., Rajbongshi and Gogoi, 2020). Regardless, both overpressured and hydrate occurrence simulations show that heavy hydrocarbon gases, methane and CO_2 require migration pathways to transport fluids from deeper to shallower strata (Kong et al., 2018; Sun et al., 2020a).

In the Baiyun Sag, although the sedimentary succession is thick, igneous sills are widely distributed and their lateral terminations often coincide with normal faults or gas chimneys (Figs. 6, 7 and 9). We suggest that the interconnected network of sills, and perhaps dykes not visible in the seismic reflection data, enabled gas migration from deep sedimentary rocks to the shallow strata (see Rateau et al., 2013). In the Yunli Low Uplift, gas-rich strata are found within the differential compaction folds above volcanoes (e.g., M1, M2 and M3), which thus act as traps (Fig. 9). We suggest that faulting and fracturing generated by differential compaction folding provided gas flow pathways, aiding hydrocarbon migration that was already focused into and through the volcanoes (see Holford et al., 2017). Overall, we show free gas migrated through sills, volcanoes, normal faults and chimneys and accumulated: (i) in folded sedimentary strata below the BGHSZ (i.e. first enhanced reflections, in Figs. 9a and 14); or (ii) where only thin stratal packages overlie the buried volcanoes, the gas was able to migrate above the BGHSZ and form hydrates (Figs. 9b, c and 14). The paleo channels/turbidites of the migrating canyons also provide coarse-grained sediments at the BGHSZ, which provide favorable reservoirs for gas hydrate accumulations (Jin et al., 2020a; Zhang et al., 2020b). High geothermal gradients developed locally in the vicinity of the volcanoes, caused the BGHSZ to be locally shallower, thus allowing pluming BSRs to develop (Fig. 14). Overall, we present evidence suggesting that volcanic systems may influence gas hydrate and free gas occurrence and accumulation in two aspects: (i) promoting fluid migration pathways; (ii) temperature anomalies.

6. Conclusions

Newly acquired three-dimensional (3D) seismic reflection data from the Baiyun Sag and Yunli Low Uplift reveal that volcanic systems influence the occurrence and accumulation of gas hydrate and free gas in the Pearl River Mouth Basin, South China Sea. The buried volcanic complexes and igneous sills were formed between 23.8-15.5 Ma, followed by the development of fluid migration pathways consisting of overlying faults and gas chimneys, partly in response to differential compaction. The accumulation zones of gas hydrate and free gas widely overlap with the mapped distribution of volcanoes and sills. This free gas and gas hydrate are commonly associated with fluid migration pathways, and are occasionally trapped by differential compaction folds formed above the volcanoes or in local coarse-grained sedimentary rocks in the submarine canyon system above the sills. Volcanoes and sills likely facilitated cross-strata migration of hydrocarbon gas from deep sources and into supra-sill faults, supra-volcano faults, and gas chimneys that connected to to shallower reservoirs. Pluming bottom simulating reflectors (BSRs) occur in shallow strata above the summit of buried volcanoes, and may be formed by the local high geothermal gradients related to the release of hydrothermal fluids from the volcanoes. This study supports a growing body of work that shows volcanic systems may influence fluid migration and accumulation in sedimentary basins long after magmatic activity has ceased.

Declaration of Competing Interest

Acknowledgments

We would like to acknowledge the China National Offshore Oil Company, which acquired and processed the 3D seismic data. This study was supported by the Strategic Priority Research Program of the Chinese Academy of Sciences (No. XDB42020100), the Marine S&T Fund of Shandong Province for Pilot National Laboratory for Marine Science and Technology(Qingdao)（No.2021QNLM020002), National Natural Science Foundation of China Innovation Group Project (42121005), Laboratory for Marine Science and Technology (Qingdao) Initial Foundation (JCZX202019)，National Key R&D Program of China (2017YFC0307301-1), and Pilot National, and Research start-up funds of Zhufeng Scholars Program.

Data availability

Research data to this article can be found online at https://drive.google.com/file/d/1aHTs_fmMAU7WZwETEA1OH3G-LnMW0G9E/view?usp=sharing.

References

Biastoch, A., Treude, T., Rüpke, L.H., Riebesell, U., Roth, C., Burwicz, E.B., Park,W., Latif, M., Böning, C.W., Madec, G., Wallmann, K., 2011. Rising Arctic Ocean temperatures cause gas hydrate destabilization and ocean acidification. Geophysics Research Letters. 38 (8): L08602. https://doi.org/10.1029/2011gl047222.

Capriolo, M., Marzoli, A., Aradi, A.L., Ackerson, M.R., Bartoli, O., Callegaro, S., Corso, J.D., Ernesto, M., Vasconcellos, E.M.G., Min, A.D., Newton R.J., Szabó4, C., 2021. Massive methane fluxing from magma-sediment interaction in the end-Triassic Central Atlantic Magmatic Province. Nature Communication. 12, 5534. https://doi.org/10.1038/s41467-021-25510-w.

Cheng, C., Jiang, T., Kuang, Z.G., Yang, C.Z., Zhang, C., He, Y.L., Cheng, Z., Tian, D.M., Xiong, P.F., 2020. Characteristics of gas chimneys and their implications on gas hydrate accumulation in the Shenhu area, northern South China Sea. Journal of Natural Gas Science and Engineering. 84, 103629. https://doi.org/10.1016/j.jngse.2020.103629.

Clift, P.D., Lin, J., 2001. Preferential mantle lithospheric extension under the South China margin. Marine and Petroleum Geology. 18(8), 929-945. https://doi.org/10.1016/S0264-8172(01)00037-X.

Collett, T.S., Johnson, A.H., Knapp, C.C., Boswell, R., 2009. Natural Gas Hydrates: A Review, in T. Collett, A. Johnson, C. Knapp, and R. Boswell, eds., Natural gas hydrates-Energy resource potential and associated geologic hazards: AAPG

Memoir, 89, 146-219.

Cosgrove, J.W., Hillier, R.D., 1999. Forced-fold development within Tertiary sediments of the Alba Field, UKCS: evidence of differential compaction and post-depositional sandstone remobilization. Geological Society. 169(1), 61-71. https://doi.org/10.1144/GSL.SP.2000.169.01.05.

Daigle, H., Dugan, B., 2014. Pore size controls on the base of the methane hydrate stability zone in the Kumano Basin, offshore Japan. Geophysical Research Letter. 41, 8021-8028. http://dx.doi.org/10.1002/2014GL062135.

Dasgupta, R., Hirschmann, M.M., 2010. The deep carbon cycle and melting in Earth's interior. Earth and Planetary Letters. 298, 1-13. http://dx.doi.org/10.1016/j.epsl.2010.06.039.

Deng, P., Mei, L.F., Liu, J., Zheng, J.Y., Liu, M.H., Cheng, Z.J., Guo, F.T., 2019. Episodic normal faulting and magmatism during the syn-spreading stage of the Baiyun sag in Pearl River Mouth Basin: Response to the multi-phase seafloor spreading of the South China Sea. Marine Geophysical Research. 40(1), 33-50. https://doi.org/10.1007/s11001-018-9352-9.

Ding, W.W., Sun, Z., Dadd, K., Fang, Y., Li, J., 2018. Structures within the oceanic crust of the central South China Sea basin and their implications for oceanic accretionary processes. Earth and Planetary Science Letters. 488, 115-125. https://doi.org/10.1016/j.epsl.2018.02.011.

Ding, W.W., Sun, Z., Mohn, G., Nirrengarten, M., Tugend, J., Manatschal, G., Li, J.B., 2020. Lateral evolution of the rift-to-drift transition in the South China Sea:

Evidence from multi-channel seismic data and IODP Expeditions 367&368 drilling results. Earth and Planetary Science Letters. 531, 115932. https://doi.org/10.1016/j.epsl.2019.115932.

Dong, D.D., Zhang, G.C., Zhong, K., Yuan, S.Q., Wu, S.G., 2009. Tectonic evolution anddynamics of deepwater area of Pearl River Mouth Basin, northern South China Sea (Chinese in English Abstract). Journal of Earth Science. 20, 147-159.

Fang, Y.X., Lu, J.A. Liang, J.Q., Kuang, Z.G., Cao, Y.C., Chen, D.F., 2019. Numerical studies of gas hydrate evolution time in Shenhu area in the northern South China Sea. China Geology. 1, 49-55. https://doi.org/10.1016/j.cngeo.2019.01.001.

Franke, D., 2013. Rifting, lithosphere breakup and volcanism: comparison of magma□poor and volcanic rifted margins. Marine and Petroleum Geology. 43, 63-87. https://doi.org/10.1016/j.marpetgeo.2012.11.003.

Grove, C. 2013. Submarine hydrothermal vent complexes in the Paleocene of the Faroe-Shetland Basin: Insights from three-dimensional seismic and petrographical data. Geology. 41(1), 71-74. https://doi.org/10.1130/G33559.1.

Hayes, D.E., Nissen, S.S., 2005. The South China Sea margins: Implications for rifting contrasts. Earth and Planetary Science Letters. 237(3-4), 601-616. https://doi.org/10.1016/j.epsl.2005.06.017.

Holbrook, W.S., Hoskins, H., Wood, W.T., Stephen, R.A., Lizarralde, D., 1996. Methane hydrate and free gas on the Blake Ridge from vertical seismic profiling. Science 80 (273), 1840-1843.

Holford, S.P., Schofield, N., Reynolds, P., 2017. Subsurface fluid flow focused by buried volcanoes in sedimentary basins: Evidence from 3D seismic data, Bass Basin, offshore southeastern Australia. Interpretation. 5(3), SK39-SK50. https://doi.org/10.1190/int-2016-0205.1.

Hornbach, M.J., Saffer, D.M., Holbrook,W.S., VanAvendonk, H.J.A., Gorman, A.R. 2008. Three-dimensional seismic imaging of the Blake Ridge methane hydrate province: evidence for large, concentrated zones of gas hydrate and morphologically driven advection. Journal of Geophysical Research. 113 (B7): B07101. https://doi.org/10.1029/2007jb005392.

Hou, Z.Q., Zaw, K., Li, Y.H., Zhang, Q.L., Zeng, Z.G., Urabe, T., 2005. Contribution of magmatic fluid to the active hydrothermal system in the JADE field, Okinawa trough: evidence from fluid inclusions, oxygen and helium isotopes. International Geology Review. 47(4), 420-437. https://doi.org/10.2747/0020-6814.47.4.420.

Infante-Paez, L., and Marfurt, K.J., 2017. Seismic expression and geomorphology of igneous bodies: A Taranaki Basin, New Zealand, case study. Interpretation. 5(3), SK121-SK140. https://doi.org/10.1190/INT-2016-0244.1.

Jamtveit, B., Svensen, H., Podladchikov, Y.Y., Planke, S., 2004. Hydrothermal vent complexes associated with sill intrusions in sedimentary basins. Journal of Empirical Theology. 234(1), 233-241. https://doi.org/10.1016/j.epsl.2005.06.017.

Jin, J.P., Wang, X.J., Guo, Y.Q., Li, J. Li, Y.P., Zhang, X., Qian, J., Sun, L.Y., 2020a. Geological controls on the occurrence of recently formed highly concentrated gas hydrate accumulations in the Shenhu area, South China Sea. Marine and

Petroleum Geology. 116, 104294. https://doi.org/10.1016/j.marpetgeo.2020.104294.

Jin, J.P., Wang, X.J., He, M., Li, J., Yan, C.Z., Li, Y.P., Zhou, J.L., Qian, J., 2020b. Downward shift of gas hydrate stability zone due to seafloor erosion Dongsha Island, South China Sea. Journal of Oceanology Limology. 38, 1188-1200. https://doi.org/10.1007/s00343-020-0064-z.

Kong, L.T., Chen, H.H., Ping, H.W., Zhai, P.Q., Liu, Y.H., Zhu, J.Z., 2018. Formation pressure modeling in the Baiyun Sag, northern South China Sea: Implications for petroleum exploration in deep-water areas. Marine and Petroleum Geology. 97, 154-168. https://doi.org/10.1016/j.marpetgeo.2018.07.004.

Li, C.F., Xu, X., Lin, J., Sun, Z., et al., 2014. Ages and magnetic structures of the South China Sea constrained by the deep tow magnetic surveys and IODP Expedition 349. Geochemistry Geophysics Geosystems. 15, 4958-4983. https://doi.org/10.1002/2014GC005567.

Li, P., Rao, C., 1994. Tectonic characteristics and evolution history of the Pearl river mouth basin. Tectonophysics. 235, 13-25. https://doi.org/10.1016/0040-1951(94)90014-0.

Li, J., Lu, J.A., Kang, D.J., Ning, F.L., Lu, H.F., Kuang, Z.G., Wang, D.D., Liu, C.L., Hu, G.W., Wang, J.S., Liang, J.Q., 2019. Lithological characteristics and hydrocarbon gas sources of gas hydrate bearing sediments in the Shenhu area, South China Sea: implications from the W01B and W02B sites. Marine Geology. 408, 36-47. https://doi.org/10.1016/j.margeo.2018.10.013.

Lüdmann, T., Wong, H.K., 1999. Neotectonic regime at the passive continental margin of northern South China Sea. Tectonophysics 311, 113-138. https://doi.org/10.1016/S0040-1951(99)00155-9.

Omosanya, K.O., Eruteya, O. E., Siregar, E.S.A., Zieba, K.J., Johansen, S.E., Alves, T.M., Waldmann, N.D., 2018. Three-dimensional (3-D) seismic imaging of conduits and radial faults associated with hydrothermal vent complexes (Voring Basin, Offshore Norway). Marine Geology. 399, 115-134. https://doi.org/10.1016/j.margeo.2018.02.007.

Pang, X., Chen, C.M., Peng, D.Y., Zhou, D., Shao, L., He, M., Liu, B.J., 2008. Basic geology of Baiyun deep-water area in the northern South China Sea (in Chinese with English abstract). Chinese Offshore Oil and Gas. 20, 215-222.

Phillips, T.B., Magee, C., 2020. Structural controls on the location, geometry and longevity of an intraplate volcanic system: the Tuatara Volcanic Field, Great South Basin, New Zealand. Journal of the Geological Society. 177(5), 1039-1056. https://doi.org/10.1144/jgs2020-050.

Planke, S., Rasmussen, T., Rey, S.S., Myklebust, R., 2005. Seismic characteristics and distribution of volcanic intrusions and hydrothermal vent complexes in the Vøring and Møre basins. In: Petroleum Geology: North-West Europe and Global Perspectives. 6, 833-844. https://doi.org/10.1144/0060833.

Planke, S., Millett, J.M., Maharjan, D., Jerram, D.A., Abdelmalak, M.M., Groth, A., Hoffmann, J., Berndt, C., Myklebust, R., 2017. Igneous seismic geomorphology of buried lava fields and coastal escarpments on the Vøring volcanic rifted margin. Interpretation. 5(3), SK161-SK177. https://doi.org/10.1190/int-2016-0164.1.

Portnov, A., Cook, A.E., Heidari, M., Sawyer, D.E., Santra, M., Nikolinakou, Maria., 2020. Salt-driven evolution of a gas hydrate reservoir in Green Canyon, Gulf of Mexico. AAPG Bulletin. 104 (9), 1903-1919. https://doi.org/10.1306/10151818125.

Portnov, A., Cook, A.E., Vadakkepuliyambatta, S., 2021. Diverse gas composition controls the Moby-Dick gas hydrate system in the Gulf of Mexico. Geology. 49(12), 1446-1451. https://doi.org/10.1130/G49310.1.

Qian, J., Wang, X.J., Collett, T. S., Guo, Y.Q., Kang, D.J., Jin, J.P., 2018. Downhole log evidence for the coexistence of structure II gas hydrate and free gas below the bottom simulating reflector in the South China Sea. Marine and Petroleum Geology. 98, 662-674. https://doi.org/10.1016/j.marpetgeo.2018.09.024.

Qin, G.Q., 2000. Comments on “Discussion on the Upper-Lower Tertiary boundary in Well BY7-1” of the Pearl River Mouth Basin (in Chinese with English Abstract). Journal of Stratigraphy. 24, 387-393.

Rajbongshi, A., Gogoi, S.B., 2020. A Review of Microbial Degradation of Petroleum Hydrocarbons. In Advances in Petroleum Technology, 1st ed. Jenny Stanford Publishing, America, 8-10.

Rateau, R., Schofield, N., Smith, M., 2013. The potential role of igneous intrusions on hydrocarbon migration, West of Shetland. Petroleum Geoscience. 19(3), 259-272. https://doi.org/10.1144/petgeo2012-035.

Rupple, C.D., Kessler, J.D., 2017. The interaction of climate change and methane hydrates. Reviews of Geophysics. 55(1), 126-168. https://doi.org/10.1002/2016rg000534.

Sakai, H., Gamo, T., Kim, E.S., Tsutsumi, M., Tanaka, T., Ishibashi, J.I., Wakita, H., Yamano, M., Oomori, T., 1990. Venting of Carbon Dioxide-Rich Fluid and Hydrate Formation in Mid-Okinawa Trough Backarc Basin. Science. 248(4959), 1093-1096. https://doi.org/10.1126/science.248.4959.1093.

Schutter, S.R., 2003. Hydrocarbon occurrence and exploration in and around igneous rocks. Geological Society London Special Publications. 214, 7-33. https://doi.org/10.1144/GSL.SP.2003.214.01.02.

Shedd, W., Boswell, R., Frye, M., Godfriaux, P., Kramer, K., 2012. Occurrence and nature of "bottom simulating reflectors" in the northern Gulf of Mexico. Marine and Petroleum Geology. 34, 31-40. https://doi.org/10.1016/j.marpetgeo.2011.08.005

Shipley, T.H., Houston, M.H., Buffler, R.T., Shaub, F.J., Mcmillen, K.J., Ladd, J.W., 1979. Seismic evidence for widespread possible gas hydrate horizons on continental slopes and rises. AAPG Bulletin. 63, 2204-2213. https://doi.org/10.1306/2f91890a-16ce-11d7-8645000102c1865d.

Sloan, E.D., Koh, C.A., 2017. Clathrate Hydrates of Natural Gases, 3rd ed. CRC Press, Boca Raton, America, 10-18.

Snyder, G.T., Sano, Y.J., Naoto, T., Matsumoto, R., Kakizaki, Y., Tomaru, H., 2020. Magmatic fluids play a role in the development of active gas chimneys and massive gas hydrates in the Japan Sea. Chemical Geology. 535, 119462. https://doi.org/10.1016/j.chemgeo.2020.119462.

Song, X.X., Li, C.F., Yao, Y.J., Shi, H.S., 2017. Magmatism in the evolution of the South China Sea: Geophysical characterization. Marine Geology. 394, 4-15. https://doi.org/10.1016/j.margeo.2017.07.021.

Su, D., White, N., McKenzie, D.A.N., 1989. Extension and subsidence of the Pearl River Mouth basin, northern South China Sea. Basin Research. 2, 205-222. https://doi.org/10.1111/j.1365-2117.1989.tb00036.x.

Su, P.B., Liang, J.Q., Peng, J., Zhang, W., Xu J.H., 2018. Petroleum systems modeling on gas hydrate of the first experimental exploitation region in the Shenhu area, northern South China sea, Journal of Asian Earth Sciences. 168, 57-76. https://doi.org/10.1016/j.jseaes.2018.08.001.

Sun, L.Y., Wang, X.J., He, M., Jin, J.P., Li, J., Li, Y.P., Zhu, Z.Y., 2020a. Thermogenic gas controls high saturation gas hydrate distribution in the Pearl River Mouth Basin: Evidence from numerical modeling and seismic anomalies. Ore Geology Review. 127, 1-16. http://dx.doi.org/10.1016/j.oregeorev.2020.103846.

Sun, Q.L., Wu, S.G., Cartwright, J., Dong, D.D., 2012. Shallow gas and focused fluid flow systems in the Pearl River Mouth Basin, northern South China Sea. Marine Geology. 315, 1-14. https://doi.org/10.1016/j.margeo.2012.05.003.

Sun, Q.L., Wu, S.G., Cartwright, J., Wang, S.H., Lu, Y.T., Chen, D.X., Dong, D.D., 2014. Neogene igneous intrusions in the northern South China Sea: Evidence from high-resolution three dimensional seismic data. Marine and Petroleum

Geology. 54, 83-95. http://dx.doi.org/10.1016/j.marpetgeo.2014.02.014.

Sun, Q.L., Jackson, C.A., Magee, C., Xie, X.N., 2020b. Deeply buried ancient volcanoes control hydrocarbon migration in the South China Sea. Basin Research. 32(1), 146-162. http://dx.doi.org/10.31223/osf.io/trsv4.

Sun, Q.L., Magee, C., Jackson, C.A.L., Mitchell, S.J., Xie, X.N., 2020c. How do deep-water volcanoes grow? Earth and Planetary and Science Letters. 542, 1-14. http://dx.doi.org/10.1016/j.epsl.2020.116320.

Sun, Q.L., Tiago, M.A., Zhao, M.H., Jean-Claude, S., Gérôme, C., Xie, X.N., 2020d. Post-rift magmatism on the northern South China Sea margin. Geological Society of American Bulletin. 132(11-12), 2382-2396. https://doi.org/10.1130/B35471.1.

Sun, Q.L., Wang, C., Xie, X.N., 2022a. Sill swarms and hydrothermal vents in the Qiongdongnan Basin, northern South China Sea. Geosystems and Geoenvironment. 1(2): 100037. https://doi.org/10.1016/j.geogeo.2022.100037.

Sun, Q.L., Alves, T.M., Wu, S.G., Zhao, M.H., Xie, X.N., 2022b. Early Miocene magmatism in the Baiyun Sag (South China Sea): A view to the origin of intense post-rift magmatism. Gondwana Research. https://doi.org/10.1016/j.gr.2022.05.013.

Sun, Z., Lin, J., Qiu, N., Jian, Z.M., Wang, P.X., Pang, X., Zheng, J.Y., Zhu, B.D., 2019. The role of magmatism in the thinning and breakup of the South China Sea continental margin. National Science Review. 6(5), 871-876. https://doi.org/10.1093/nsr/nwz116.

Svensen, H., Jamtveit, B., Planke, S., Chevallier, L., 2006. Structure and evolution of hydrothermal vent complexes in the Karoo Basin, South Africa. Journal of the Geological Society. 163, 671-682. http://dx.doi.org/10.1144/1144-764905-037.

Svensen, H., Planke, S., Malthe-Sørenssen, A. Jamtveit, B., Myklebust, R., Eidem, T.R., Rey, S.S., 2004. Release of methane from a volcanic basin as a mechanism for initial Eocene global warming. Nature 429, 542-545. https://doi.org/10.1038/nature02566.

Trude, J., Cartwright, J., Davies, R.J., Smallwood, J., 2003. New technique for dating igneous sills. Geology. 31, 813-816.

Torres, M.E., Wallmann, K., Tréhu A.M., Bohrmann, G., Borowski, W.S., Tomaru, H., 2004. Gas hydrate growth, methane transport, and chloride enrichment at the southern summit of Hydrate Ridge, Cascadia margin off Oregon. Earth and Planetary Science Letters. 226, 1-2, 225-241. https://doi.org/10.1016/j.epsl.2004.07.029.

Wang, X.J., Hutchinson, D.R., Wu, S.G., Yang, S.X., Guo, Y.Q., 2011. Elevated gas hydrate saturations within silt and silty-clay sediments in the Shenhu area, South China Sea. Journal of Geophysical Research: Atmospheres. 116(5), B05102. http://dx.doi.org/c10.1029/2010JB007944.

Wang, X.J., Collett, T.S., Lee, M., Yang, S.X., Guo, Y.Q., Wu, S.G., 2014. Geological controls on the occurrence of gas hydrate from core, downhole log, and seismic data in the Shenhu area, South China Sea. Marine Geology. 357, 272-292. https://doi.org/10.1016/j.margeo.2014.09.040.

Wang, X.J., Qian, J., Collett T. S., Shi, H. S., Yang, S. X., Yan, C. Z., Li, Y. P., Wang, Z. Z., Chen, D. X., 2016. Characterization of gas hydrate distribution using conventional 3D seismic data in the Pearl River Mouth Basin, South China Sea. Interpretation, 4(1), SA25-SA37. http://dx.doi.org/10.1190/INT-2015-0020.1.

Wang, P.C., Li, S.Z., Suo, Y.H., Guo, L.L., Santosh, M., Li, X.Y., Wang, G.Z., Jiang, Z.X., Liu, B., Zhou, J., Jiang, S.H., Cao, X.Z., Liu, Z., 2021. Structural and kinematic analysis of Cenozoic rift basins in South China Sea: A synthesis. Earth Science Reviews. 216, 103522. https://doi.org/10.1016/j.earscirev.2021.103522.

Wang, C., Sun, Q.L., Xie, X.N., 2022. Sediment deformation triggered by underlying magma intrusion. Journal of Asian Earth Sciences. 225: 105045. https://doi.org/10.1016/j.jseaes.2021.105045.

Wei, J.G., Fang, Y.X., Lu, H.L., Lu, H.F., Lu, J.G., Liang, J.Q., Yang, S.X., 2018. Distribution and characteristics of natural gas hydrates in the Shenhu Sea Area, South China Sea. Marine and Petroleum Geology. 98, 622-628. http://dx.doi.org/10.1016/j.marpetgeo.2018.07.028.

Witte, J., Bonora, M., Carbone, C., Oncken, O., 2012. Fracture evolution in oil-producing sills of the Rio Grande Valley, northern Neuquén Basin, Argentina. American Association of Petroleum Geologists Bulletin. 96, 1253–1277.

Wu, N.Y., Yang, S.X., Wang, H.B., Liang, J.Q., Gong, Y.H., Lu, Z.Q., Wu, D.D., Guan H.X., 2009. Gas hydrate-bearing fluid influx sub-system for gas hydrate geological system in Shenhu Area, Northern South China Sea (in Chinese with English abstract). Chinese Journal of Geophysics. 52, 1641-1650.

http://dx.doi.org/10.3969/j.issn.0001-5733.2009.06.027.

Wu, N.Y., Xu, C.L., Li, A., Cao, H., Chen, Y., Zhang, X.L., Geng, W., Zhai, B., Li, Q., Sun, Z.L., 2022. Oceanic carbon cycle in a symbiotic zone between hydrothermal vents and cold seeps in the Okinawa Trough. Geosystems and Geoenvironment. 1, 100059. https://doi.org/10.1016/j.geogeo.2022.100059.

Yan, P., Deng, H., Liu, H., Zhang, Z., Jiang, Y., 2006. The temporal and spatial distribution of volcanism in the South China Sea region. Journal of Asian Earth Science. 27, 647-659. http://dx.doi.org/10.1016/j.jseaes.2005.06.005.

Yang, S.X., Zhang, M., Liang, J.Q., Lu, J., Zhang, Z., Holland, M., Schultheiss, P., Fu, S.Y., Sha, Z.B., the GMGS3 Science Team, 2015. Preliminary results of China's third gas hydrate drilling expedition: a critical step from discovery to development in the South China Sea. Fire in the Ice. 15(2), 1-5.

Yang, S.X., Liang, J.Q., Lei, Y., Gong, Y.H., Xu, H.N., Wang, H.B., Lu, J.A., Holland, M., Schultheiss, P., Wei, J.G., the GMGS4 Science Team, 2017a. GMGS4 gas hydrate drilling expedition in the South China Sea. Fire in the Ice. 17(1), 7-11.

Yang, S, Jin, Z.K., Han, J.H., 2017b. Cenozoic magmatic activities and stages in the Baiyun Sag, Northern Margin of South China Sea (in Chinese with English abstract). Marine Geology and Quaternary Geology. 37(06), 34-46.

Yoo, D.G., Kang, N.K., Yi, B.Y., Kim, Ryu, B.J., Lee, K., Lee, G.H., Riedel, M., 2013. Occurrence and seismic characteristics of gas hydrate in the Ulleung Basin, East Sea. Marine and Petroleum Geology. 47, 236-247. http://dx.doi.org/10.1016/j.marpetgeo.2013.07.001.

Zeng, Z.W., Zhu, H.T., Yang, X.H., Zhang, G. C., Zeng, H.L., 2019. Three-dimensional imaging of Miocene volcanic effusive and conduit facies: Implications for the magmatism and seafloor spreading of the South China Sea. Marine and Petroleum Geology. 109,193-207. https://doi.org/10.1016/j.marpetgeo.2019.06.024.

Zhang, H.Q., Yang, S.X., Wu, N.Y., Melanie, X.X., Peter, H.S., Kelly, R., 2007. Successful and surprising results for China first gas hydrate drilling expedition. Fire in the Ice. 7(3), 6-9.

Zhang, W., Liang, J.Q., Lu, J.A., Wei, J.G., Su, P.B., Fang, Y.X., Guo, Y.Q., Yang, S.X., Zhang, G.X., 2017. Accumulation features and mechanisms of high saturation natural gas hydrate in Shenhu area, northern South China Sea. Petroleum Exploration and Development. 44, 708-719. https://doi.org/10.1016/S1876-3804(17)30082-4.

Zhang, W., Liang, J.Q, Wan, Z.F., Su, P.B., Huang, W., Wang, L.F. Lin, L., 2020a. Dynamic accumulation of gas hydrates associated with the channel-levee system in the Shenhu area, northern South China Sea. Marine and Petroleum Geology. 117, 204354. https://doi.org/10.1016/j.marpetgeo.2020.104354.

Zhang, W., Liang, J.Q., Wei, J.G., Lu, J.A., Su, P.B., Lin L., Huang, W., Guo, Y.Q., Deng, W., Yang, X.L., Wan, Z.F., 2020b. Geological and geophysical features of and controls on occurrence and accumulation of gas hydrates in the first offshore gas-hydrate production test region in the Shenhu area, Northern South China Sea. Marine and Petroleum Geology. 114: 104191.

https://doi.org/10.1016/j.marpetgeo.2019.104191.

Zhang, C.M., Sun, Z., Manatschal, G., Pang, X., Qiu, N., Su, M., Zheng, J.Y., Li, H.B., Gu, Y.L., Zhang, J.Y., Zhao, Y.H., 2021. Syn-rift magmatic characteristics and evolution at a sediment-rich margin: Insights from high-resolution seismic data from the South China Sea. Gondwana Research. 91, 81-96. https://doi.org/10.1016/j.gr.2020.11.012.

Zhao, F., Wu, S.G., Sun Q.L., Huuse, M., Li, W., Wang, Z.J., 2014. Submarine volcanic mounds in the Pearl River Mouth Basin, northern South China Sea. Marine Geology. 355, 162-172. https://doi.org/10.1016/j.margeo.2014.05.018.

Zhao, F., Alves, T.M., Wu, Shiguo, Li, W., Huuse, M., Mi, L.J., Sun, Q.L., Ma, B.J. 2016. Prolonged post-rift magmatism on highly extended crust of divergent continental margins (Baiyun sag, South China Sea). Earth and Planetary Science Letter. 445, 79-91. https://doi.org/10.1016/j.epsl.2016.04.001.

Zhao, F., Alves, T.M., Xia, S.H., Li, W., Wang, L., Mi, L.J., Wu, S.G., Cao, J.H., Fan, C.Y., 2019. Along-strike segmentation of the South China Sea margin imposed by inherited pre-rift basement structures. Earth and Planetary Science Letter. 530, 115862. https://doi.org/10.1016/j.epsl.2019.115862.

Zhou, Z.C., Mei, L.F., Liu, J., Zheng, J.Y., Chen, L., Hao, S.H., 2018. Continentalward-dipping detachment fault system and asymmetric rift structure of the Baiyun Sag, northern South China Sea. Tectonophysics. 726, 121-136. https://doi.org/10.1016/j.tecto.2018.02.002.

Zhu, W., Huang, B., Mi, L., Wilkins, R.W.T., Fu, N., Xiao, X., 2009. Geochemistry, origin, and deep-water exploration potential of natural gases in the Pearl River Mouth and Qiongdongnan basins, South China Sea. AAPG Bulletin. 93, 741-761. https://doi.org/10.1306/02170908099.

Figure captions

Fig. 1. (a) The regional map shows the location of the Pearl River Mouth Basin, northern South China Sea, including the Baiyun sag and the Liwan sag; (b) The enlarged map is the seafloor time structure map showing the distributions of submarine canyons and volcano complex (white broken line) in the Baiyun Sag and Yunli Low Uplift. The rectangle shows to the location of Figs. 4b, 10 and 12.

Fig. 2. The Cenozoic geological column, lithology and major tectonic events for the Pearl River Mouth Basin (Modified from Pang et al., 2008; Dong et al., 2009; Ma et al., 2018).

Fig. 3. Regional seismic line (a) and the interpreted profile (b) across Sites BY6-1-1 and BY7-1-1 (Location is in Fig. 1a) show the strata horizons and distribution of the west (VCI), centre (VCII) and east (VCIII) volcanic complexes in the Baiyun Sag and Yunli Low Uplift. The VC I and VC II have been found in Zhao et al., 2016, 2019; Sun et al., 2020b.

Fig. 4. (a) 3D seismic views and (b) plane map of the interpreted time map of the top of volcano complexes III (horizon TM) show the geomorphology characteristics of buried volcanic complexes (VCIII) and gas hydrate-drilling sites. Regional normal faults presented as linear structures with sharp boundaries are also observed. The rectangles and black line show the locations of Figs. 5, 8 and Fig. 6a, b respectively.

Fig. 5. (a) Minimum amplitude attribute extracted along BGHSZ with the time windows downward 50 ms shows the free gas distribution near BGHSZ. (b) Minimum amplitude attribute

extracted from the time windows between BGHSZ and T32 shows the free gas distribution in the deeper sediments. (c) Maximum amplitude attribute and (d) average positive amplitude extracted along BGHSZ with the time windows upward 50 ms shows the gas hydrate distribution. The distribution area of free gas is larger than that of gas hydrate. The black lines show the locations of Fig. 7a,b.

Fig. 6. Regional seismic line (a) and the interpreted profile (b) show the seismic characteristics of igneous sills, free gas and gas hydrate in the Shenhu area of the Baiyun Sag. Gas hydrate-bearing sediments have high amplitude just above the BGHSZ/BSR, while free gas is shown by the enhanced reflection below the BGHSZ/BSR. The accompanying relationships can be observed between sills and free gas/gas hydrate, which are connected to supra-sill faults and chimneys. The location of seismic line is shown in Fig. 4b. (c, d) Enlarged seismic profiles show the occurrence of continuous BSR (CBSR), discontinuous BSR (DBSR), gas hydrate and free gas at Sites SH2 and W18; (e-h) Enlarged seismic profiles shows the various architectures of sills in different deep strata. The BGHSZ represents the base of gas hydrate stability zone.

Fig. 7. 3D seismic views of the magmatic sills, BSRs, gas hydrates, and corresponding high amplitude zones. (a) Perspective view of arbitrary seismic section through Sites SH2, W18, and W17 shows the line distributions of sills (red arrow); (b) Seismic profile through Sites W11 and W17 shows that supra-sill faults connect gas hydrate and free gas accumulations to the sills with high-amplitude and pull up reflections. The seismic profiles locations are shown in Fig. 5.

Fig. 8. (a) Minimum amplitude attribute extracted with the time window between BGHSZ and T40 shows the free gas distribution in the Yunli Low Uplift. The spatial distribution of three enhanced reflection layers surround the summits of three volcanoes (i.e. M1, M2 and M3), respectively. (b) Maximum amplitude attribute extracted along BGHSZ with the time window upward 50 ms shows the gas hydrate distribution in the Yunli Low Uplift. The black lines shows the locations of Fig. 9a-e.

Fig. 9. The configurations of buried volcanoes, free gas, gas hydrate and normal faults (Locations

shown in Fig. 8). in the Yunli Low Uplift. (a) The supra-volcano normal faults and first layer enhanced reflection occurred within compaction fold above the magmatic volcano (M1); (b) Blanking, supra-volcano faults, corresponding DBSR, pluming BSR and second layer enhanced reflection occurred above the magmatic volcano (M2), highlighting their closely relationships. (c) 3D visualization of horizon TM shows the distribution of magmatic volcano (M3) and corresponding pluming BSR, blanking and the third enhanced reflection occurring above the summit of M3. (d) Enlarged seismic profile shows the corresponding pluming BSR in the third enhanced reflection above M3; (e) 3D visualization of minimum amplitude attributes extracted along horizons T32, T30 and T20 show the distributions of the first, second and third enhanced reflection layers above the M1, M2 and M3, respectively. The red dash lines referring to normal faults. (f, g) Waveforms of the seafloor, high amplitude, and BSR reflections with polarity indicated.

Fig. 10. (a) Variance slices along horizon T32 show the low correlations between faults, gas chimneys, and volcanoes positions respectively, and the statistical rose diagram of faults shows NE-SW striking. (b) Geological interpretation map of the distribution of non-magmatic faults, supra-sill fault and supra-volcano faults and gas chimneys corresponding to sills and buried volcanoes. The rectangle and black line show locations of Figs. 11a and 14, respectively.

Fig. 11. (a) Variance slice of 3250 ms and (b) corresponding geological interpretation map show the radial faults distribution in the overlying sediments above the volcano (M1). The location of Fig. 11a is shown in Fig. 10a. The seismic and geological interpretation profiles (c-f) across the volcano (M1) show the development of radial faults above the summit of volcano. The red dash lines referring to supra-volcano faults.

Fig. 12. The overlapped distribution map of geological elements shows magmatic sills, volcanoes, non-magmatic faults, supra-sill fault and supra-volcano faults, free gas and potential gas hydrates in the Baiyun Sag and Yunli Low Uplift.

Fig. 13. (a-c) The calculated BGHSZ at Location 1-3 compared to the BSR indicaties the

influences of high geothermal gradient (GD) for BGHSZ above the buried volcanoes. The location1-3 have been shown in Fig. 9b and c.

Fig. 14. (a) The seismic section and the schematic model (b) across gas hydrate-drilling Site SH2 and buried submarine volcanoes showing the closely relationship between gas hydrate occurrence and magmatic complexes, comprehensive geological elements in the study area, including magmatic sills, volcano complexes (VCIII), gas migration, free gas and gas hydrate occurrence. Different types of fluids can be transported along faults and gas chimneys and accumulate in the shallow sediments. Faults and gas chimneys directly occurred within the strata above the sills and buried volcanoes. The occurrence of pluming BSR above indicates the thermodynamic influences of magmatic volcanoes for gas hydrate system.

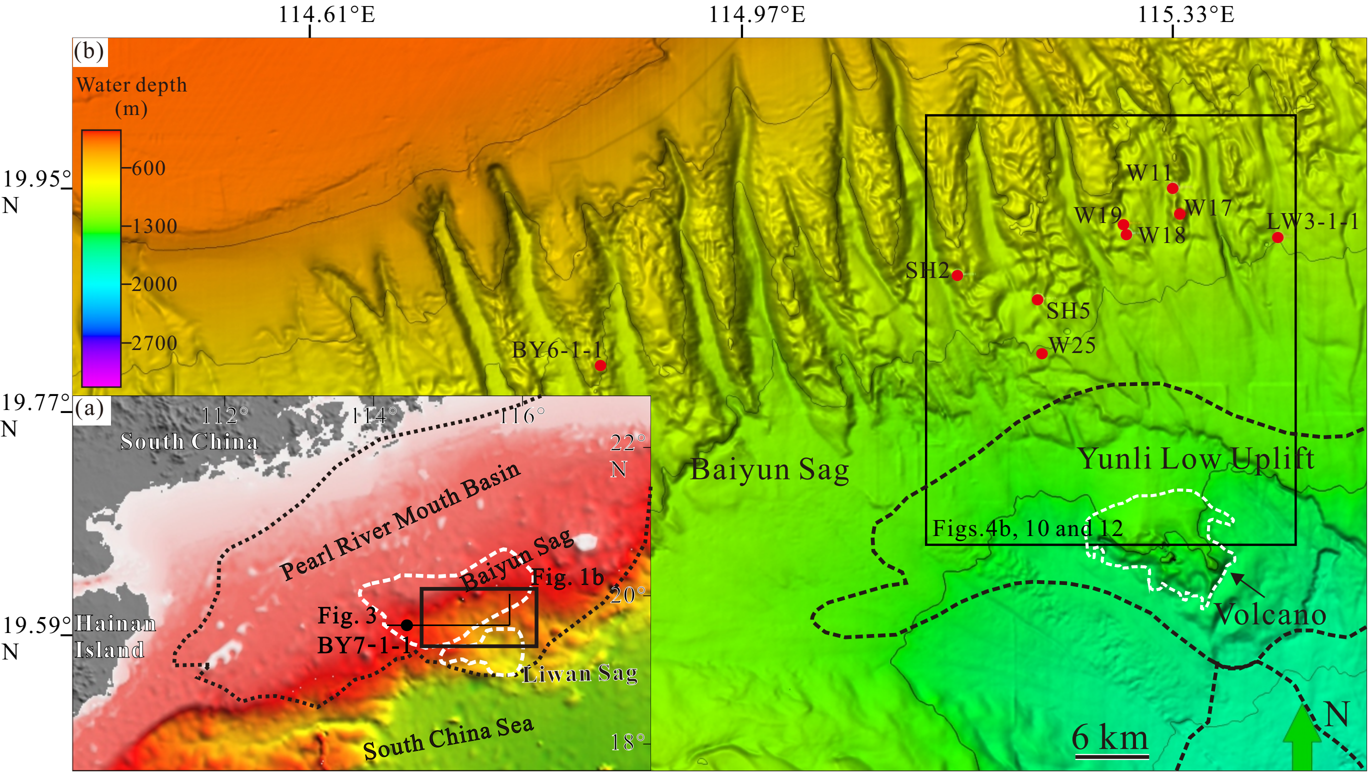
114.61°E
114.97°E
115.33°E
19.95° N
19.77° N
19.59° N
(b)
Water depth (m)
-600
-1300
-2000
-2700
W11
W17
W19
W18
LW3-1-1
SH2
SH5
W25
BY6-1-1
Baiyun Sag
Yunli Low Uplift
Figs.4b, 10 and 12
Volcano
6 km
N
(a)
112°
114°
116°
22° N
20°
18°
South China
Pearl River Mouth Basin
Baiyun Sag
Fig. 1b
Fig. 3
BY7-1-1
Hainan Island
Liwan Sag
South China Sea

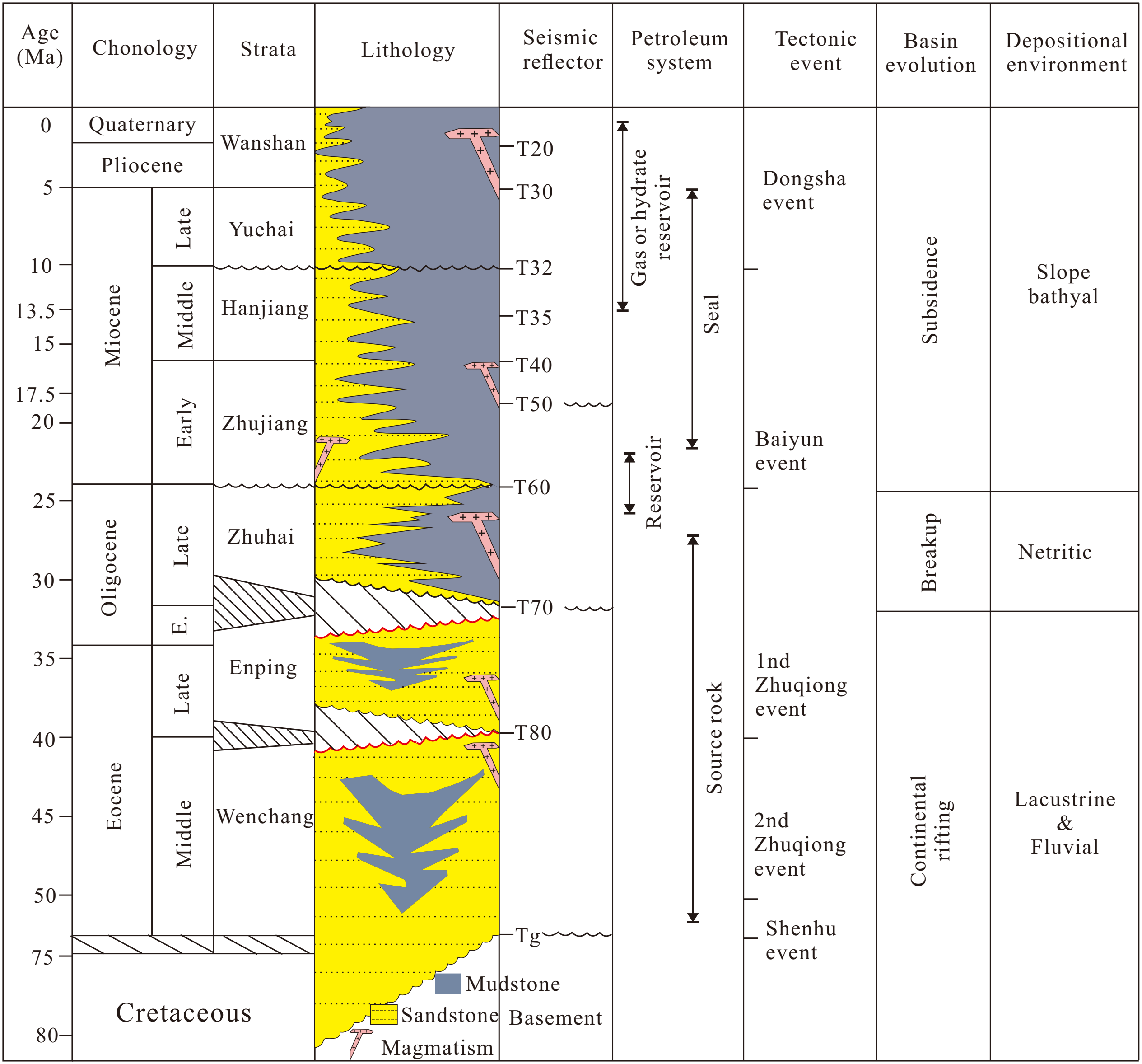
Age (Ma)
Chonology
Strata
Lithology
Seismic reflector
Petroleum system
Tectonic event
Basin evolution
Depositional environment
0
5
10
13.5
15
17.5
20
25
30
35
40
45
50
75
80
Quaternary
Pliocene
Miocene
Oligocene
Eocene
Cretaceous
Late
Middle
Early
Late
E.
Late
Middle
Wanshan
Yuehai
Hanjiang
Zhujiang
Zhuhai
Enping
Wenchang
T20
T30
T32
T35
T40
T50
T60
T70
T80
Tg
Basement
Mudstone
Sandstone
Magmatism
Gas or hydrate reservoir
Seal
Reservoir
Source rock
Dongsha event
Baiyun event
1nd Zhuqiong event
2nd Zhuqiong event
Shenhu event
Subsidence
Breakup
Continental rifting
Slope bathyal
Netritic
Lacustrine & Fluvial

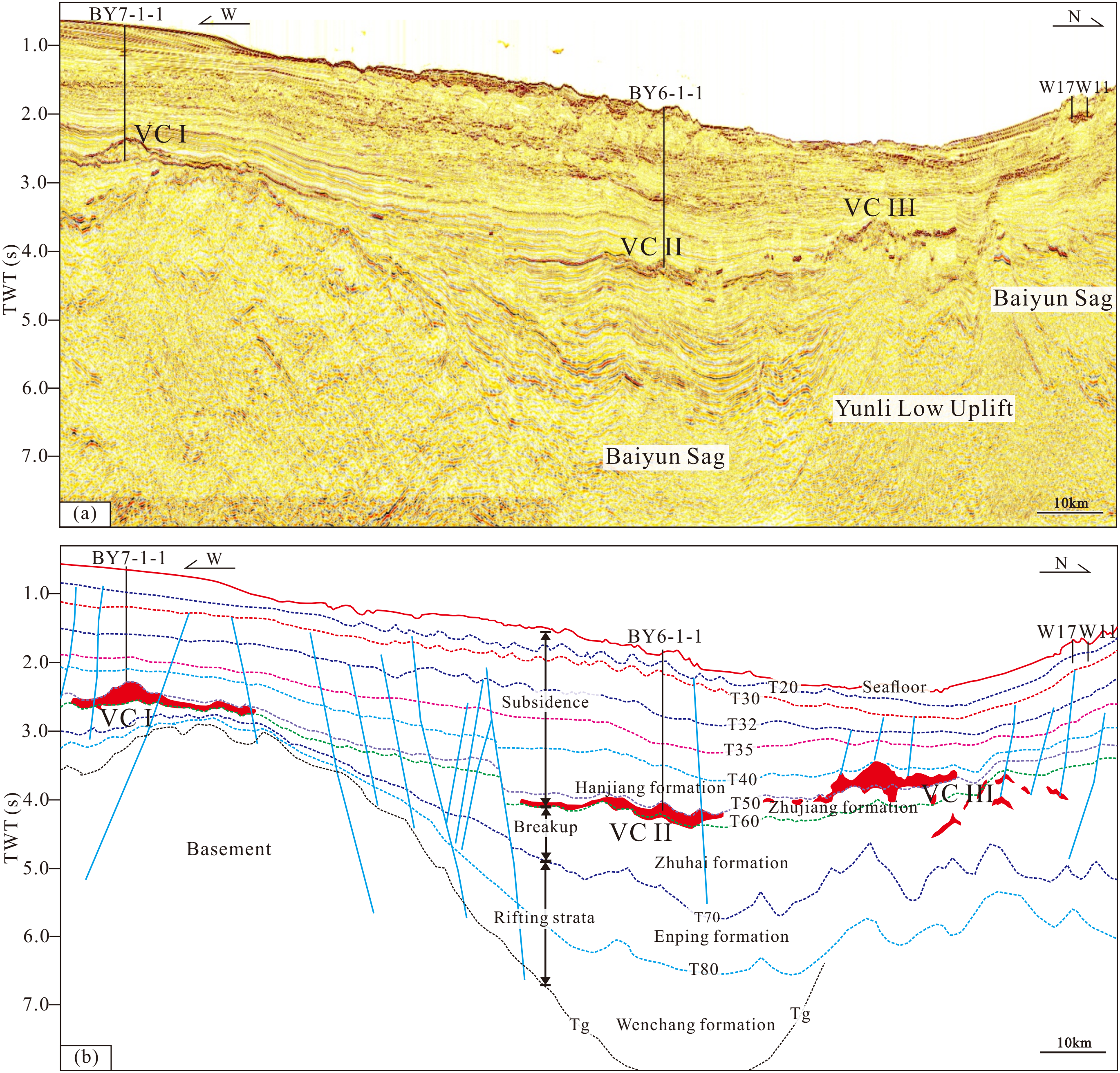
BY7-1-1
W
N
1.0
2.0
3.0
4.0
5.0
6.0
7.0
TWT (s)
VC I
BY6-1-1
W17W11
VC III
VC II
Baiyun Sag
Yunli Low Uplift
Baiyun Sag
10km
(a)
BY7-1-1
W
N
1.0
2.0
3.0
4.0
5.0
6.0
7.0
TWT (s)
BY6-1-1
W17W11
T20
Seafloor
T30
T32
T35
T40
T50
T60
T70
T80
Tg
Tg
Subsidence
Breakup
Rifting strata
Hanjiang formation
Zhujiang formation
Zhuhai formation
Enping formation
Wenchang formation
Basement
VC I
VC II
VC III
10km
(b)

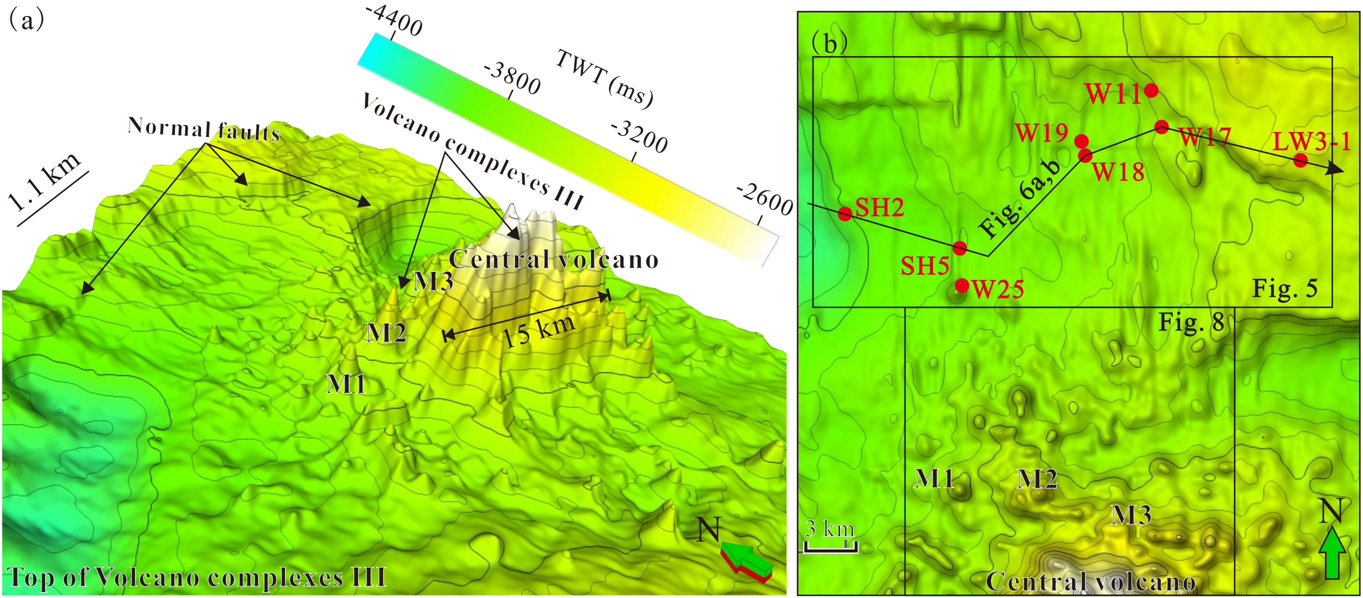
(a)
-4400
-3800
-3200
-2600
TWT (ms)
Normal faults
Volcano complexes III
1.1 km
Central volcano
M3
M2
M1
15 km
N
Top of Volcano complexes III
(b)
W11
W19
W17
LW3-1
W18
Fig. 6a,b
SH2
SH5
W25
Fig. 5
Fig. 8
M1
M2
M3
3 km
N
Central volcano

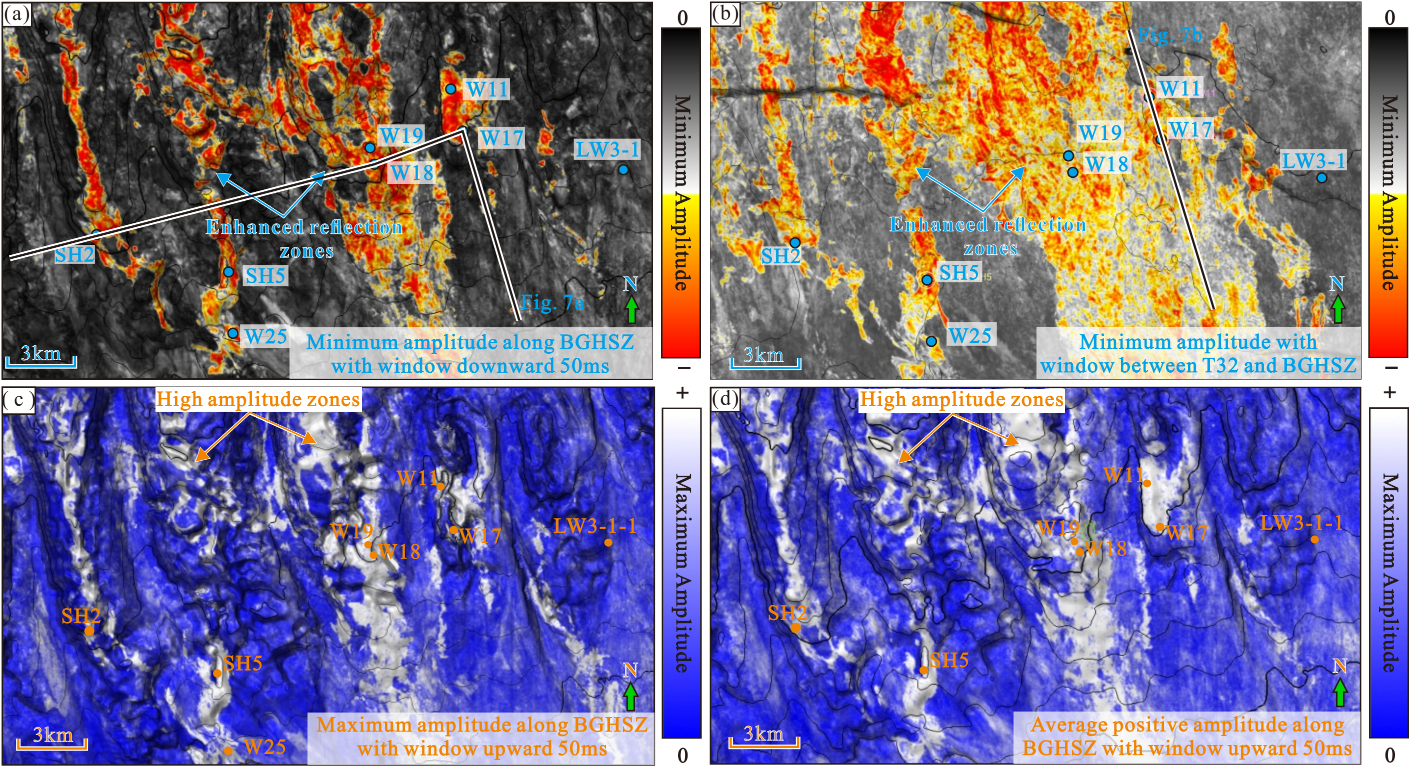(a)
W11
W19
W17
LW3-1
W18
Enhanced reflection zones
SH2
SH5
Fig. 7a
N
W25
3km
Minimum amplitude along BGHSZ with window downward 50ms
0
Minimum Amplitude
−
(b)
Fig. 7b
W11
W17
W19
W18
LW3-1
Enhanced reflection zones
SH2
SH5
W25
3km
N
Minimum amplitude with window between T32 and BGHSZ
0
Minimum Amplitude
−
(c)
High amplitude zones
W11
W19
W18
W17
LW3-1-1
SH2
SH5
N
3km
W25
Maximum amplitude along BGHSZ with window upward 50ms
+
Maximum Amplitude
0
(d)
High amplitude zones
W11
W19
W18
W17
LW3-1-1
SH2
SH5
N
3km
Average positive amplitude along BGHSZ with window upward 50ms
+
Maximum Amplitude
0

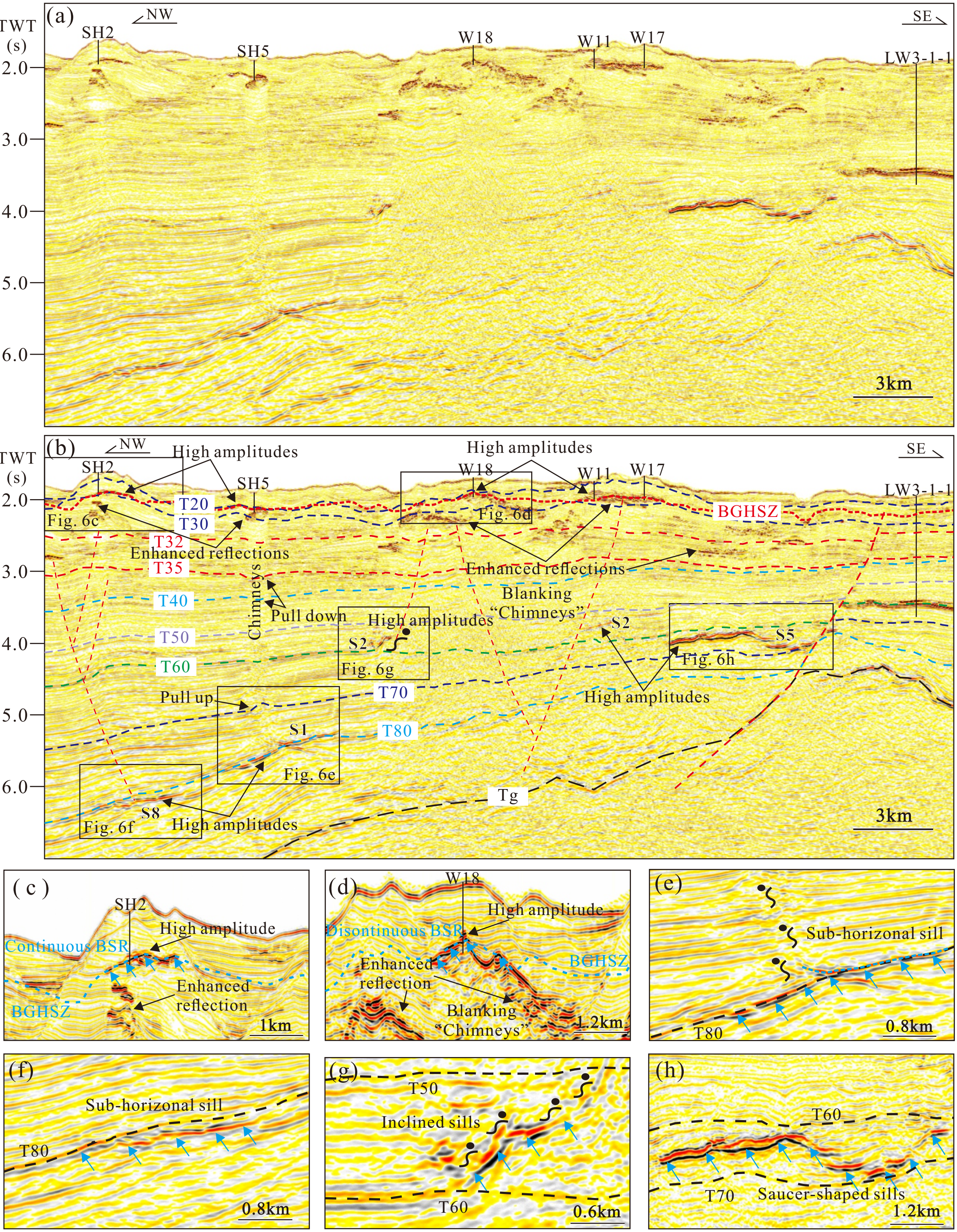
(a)
TWT (s)
NW
SE
SH2
SH5
W18
W11
W17
LW3-1-1
2.0
3.0
4.0
5.0
6.0
3km
(b)
TWT (s)
NW
SE
High amplitudes
SH2
SH5
W18
W11
W17
LW3-1-1
T20
T30
T32
T35
T40
T50
T60
T70
T80
Tg
BGHSZ
Fig. 6c
Fig. 6d
Fig. 6e
Fig. 6f
Fig. 6g
Fig. 6h
Enhanced reflections
Chimneys
Pull down
Blanking "Chimneys"
High amplitudes
S2
S2
S5
S1
S8
Pull up
High amplitudes
High amplitudes
2.0
3.0
4.0
5.0
6.0
3km
(c)
SH2
High amplitude
Continuous BSR
Enhanced reflection
BGHSZ
1km
(d)
W18
High amplitude
Disontinuous BSR
BGHSZ
Enhanced reflection
Blanking "Chimneys"
1.2km
(e)
Sub-horizonal sill
T80
0.8km
(f)
Sub-horizonal sill
T80
0.8km
(g)
T50
Inclined sills
T60
0.6km
(h)
T60
T70
Saucer-shaped sills
1.2km

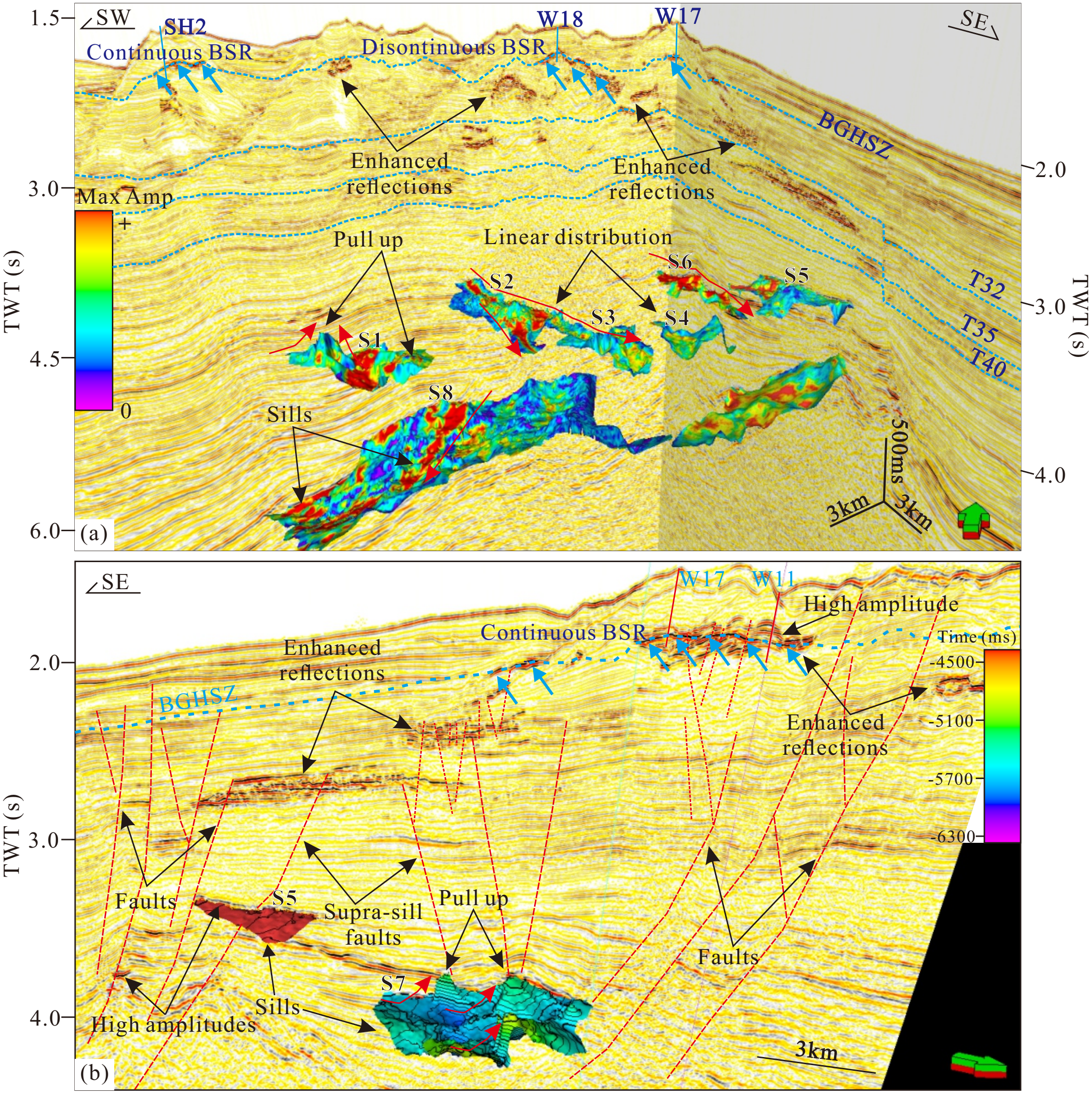
(a)
SW
SE
SH2
W18
W17
Continuous BSR
Disontinuous BSR
Enhanced reflections
Enhanced reflections
BGHSZ
Max Amp
+
0
Pull up
Linear distribution
S1
S2
S3
S4
S5
S6
S8
Sills
T32
T35
T40
500ms
3km
3km
TWT (s)
1.5
3.0
4.5
6.0
2.0
3.0
4.0
(b)
SE
W17
W11
High amplitude
Continuous BSR
Enhanced reflections
Enhanced reflections
BGHSZ
Time (ms)
-4500
-5100
-5700
-6300
Faults
S5
Supra-sill faults
Pull up
Faults
S7
Sills
High amplitudes
3km
TWT (s)
2.0
3.0
4.0

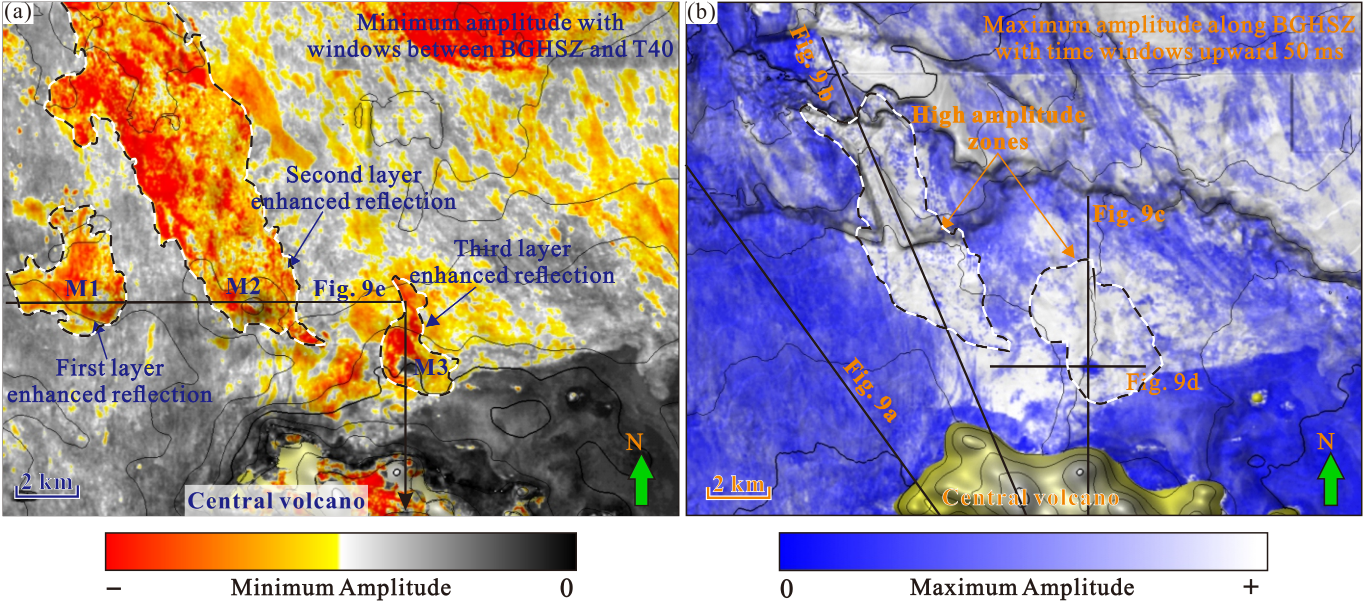

(a)
Minimum amplitude with
windows between BGHSZ and T40
Second layer
enhanced reflection
Third layer
enhanced reflection
M1
M2
M3
Fig. 9e
First layer
enhanced reflection
2 km
Central volcano
N
–
Minimum Amplitude
0
(b)
Maximum amplitude along BGHSZ
with time windows upward 50 ms
Fig. 9b
High amplitude
zones
Fig. 9c
Fig. 9d
Fig. 9a
2 km
Central volcano
N
0
Maximum Amplitude
+

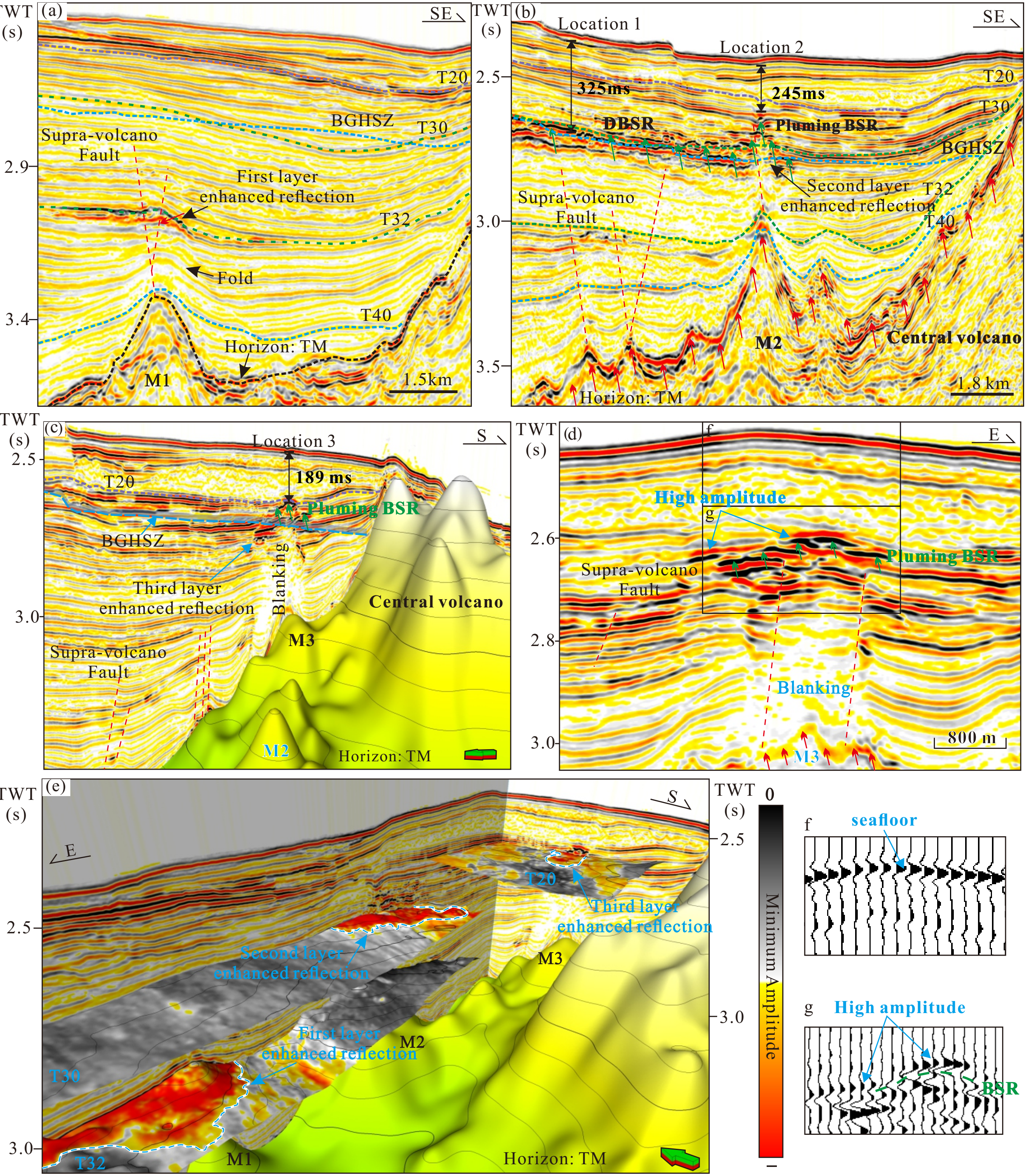
TWT (s)
(a)
SE
T20
BGHSZ
T30
Supra-volcano Fault
First layer enhanced reflection
T32
Fold
T40
Horizon: TM
M1
1.5km
2.9
3.4
(b)
Location 1
Location 2
325ms
245ms
DBSR
Pluming BSR
BGHSZ
Second layer enhanced reflection
T32
T40
Supra-volcano Fault
M2
Central volcano
Horizon: TM
1.8 km
2.5
3.0
3.5
(c)
Location 3
S
189 ms
T20
Pluming BSR
BGHSZ
Third layer enhanced reflection
Blanking
Central volcano
M3
Supra-volcano Fault
M2
Horizon: TM
(d)
E
f
g
High amplitude
Pluming BSR
Supra-volcano Fault
Blanking
M3
800 m
2.6
2.8
3.0
(e)
E
S
T20
Third layer enhanced reflection
Second layer enhanced reflection
M3
First layer enhanced reflection
M2
T30
T32
M1
Horizon: TM
0
Minimum Amplitude
−
f
seafloor
g
High amplitude
BSR

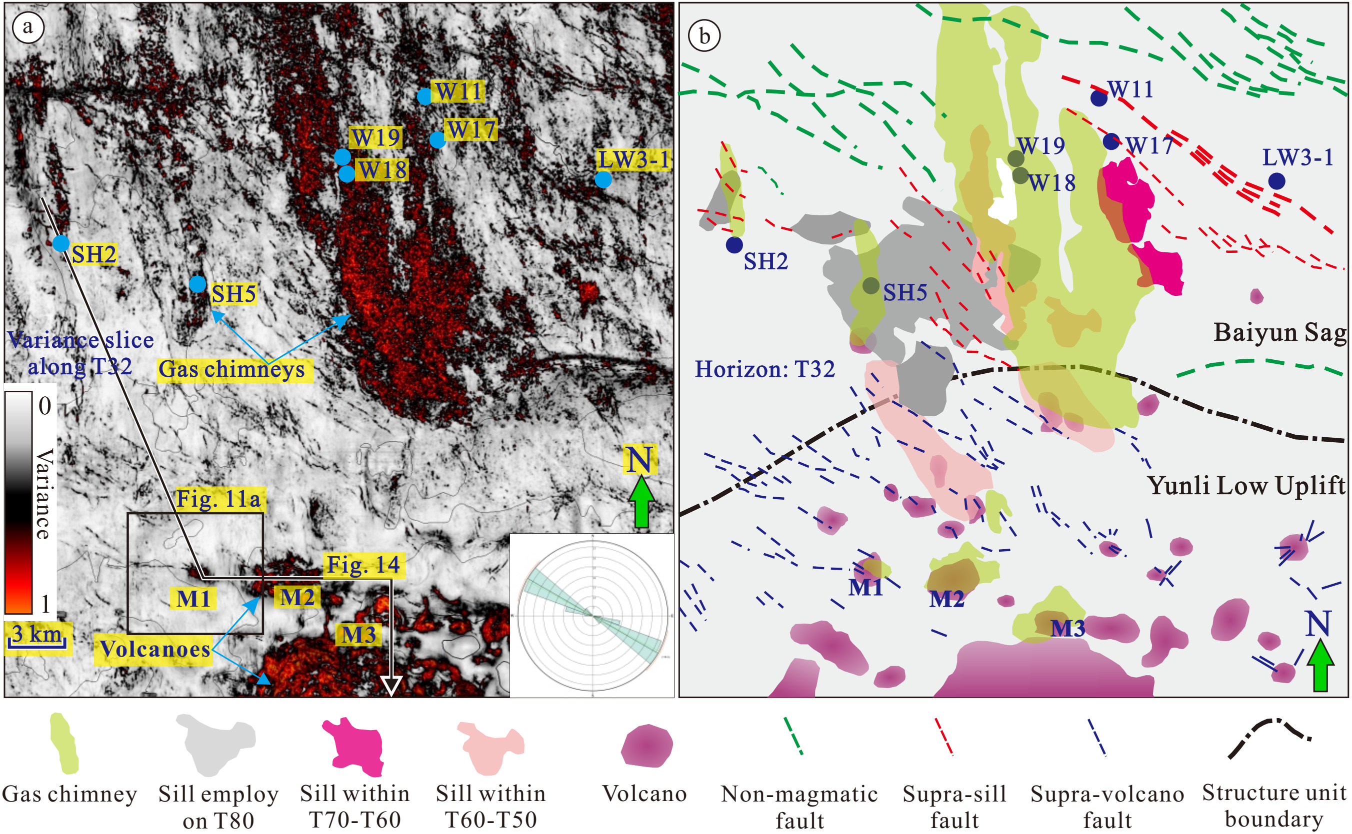
a
W11
W19
W17
W18
LW3-1
SH2
SH5
Variance slice along T32
Gas chimneys
0
Variance
1
3 km
Fig. 11a
Fig. 14
M1
M2
M3
Volcanoes
N
b
W11
W19
W17
W18
LW3-1
SH2
SH5
Horizon: T32
Baiyun Sag
Yunli Low Uplift
M1
M2
M3
N
Gas chimney
Sill employ on T80
Sill within T70-T60
Sill within T60-T50
Volcano
Non-magmatic fault
Supra-sill fault
Supra-volcano fault
Structure unit boundary

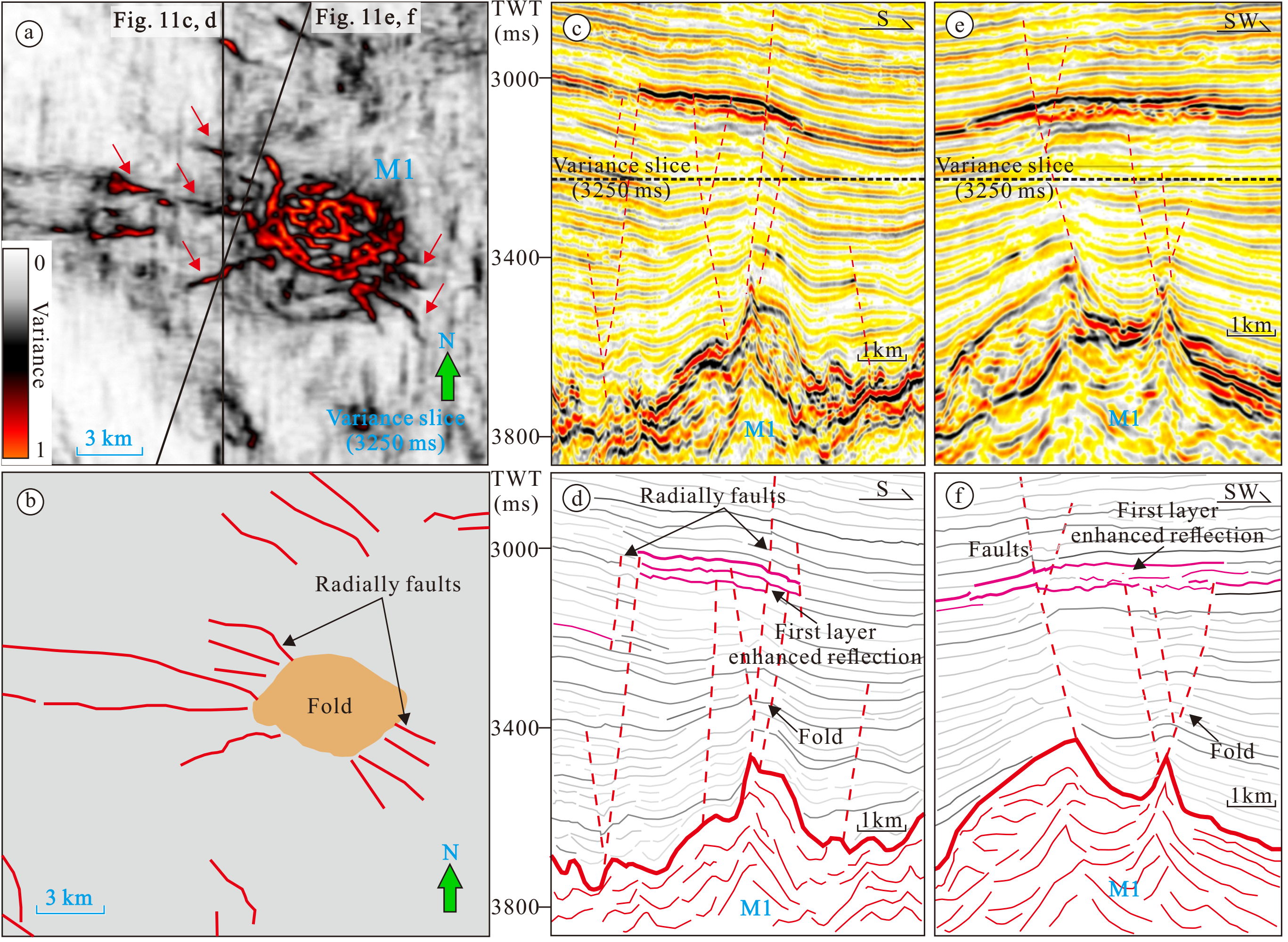
a
Fig. 11c, d
Fig. 11e, f
M1
0
Variance
1
3 km
N
Variance slice
(3250 ms)
b
Radially faults
Fold
3 km
N
TWT
(ms)
3000
3400
3800
c
S
Variance slice
(3250 ms)
1km
M1
e
SW
Variance slice
(3250 ms)
1km
M1
TWT
(ms)
3000
3400
3800
d
S
Radially faults
First layer
enhanced reflection
Fold
1km
M1
f
SW
First layer
enhanced reflection
Faults
Fold
1km
M1

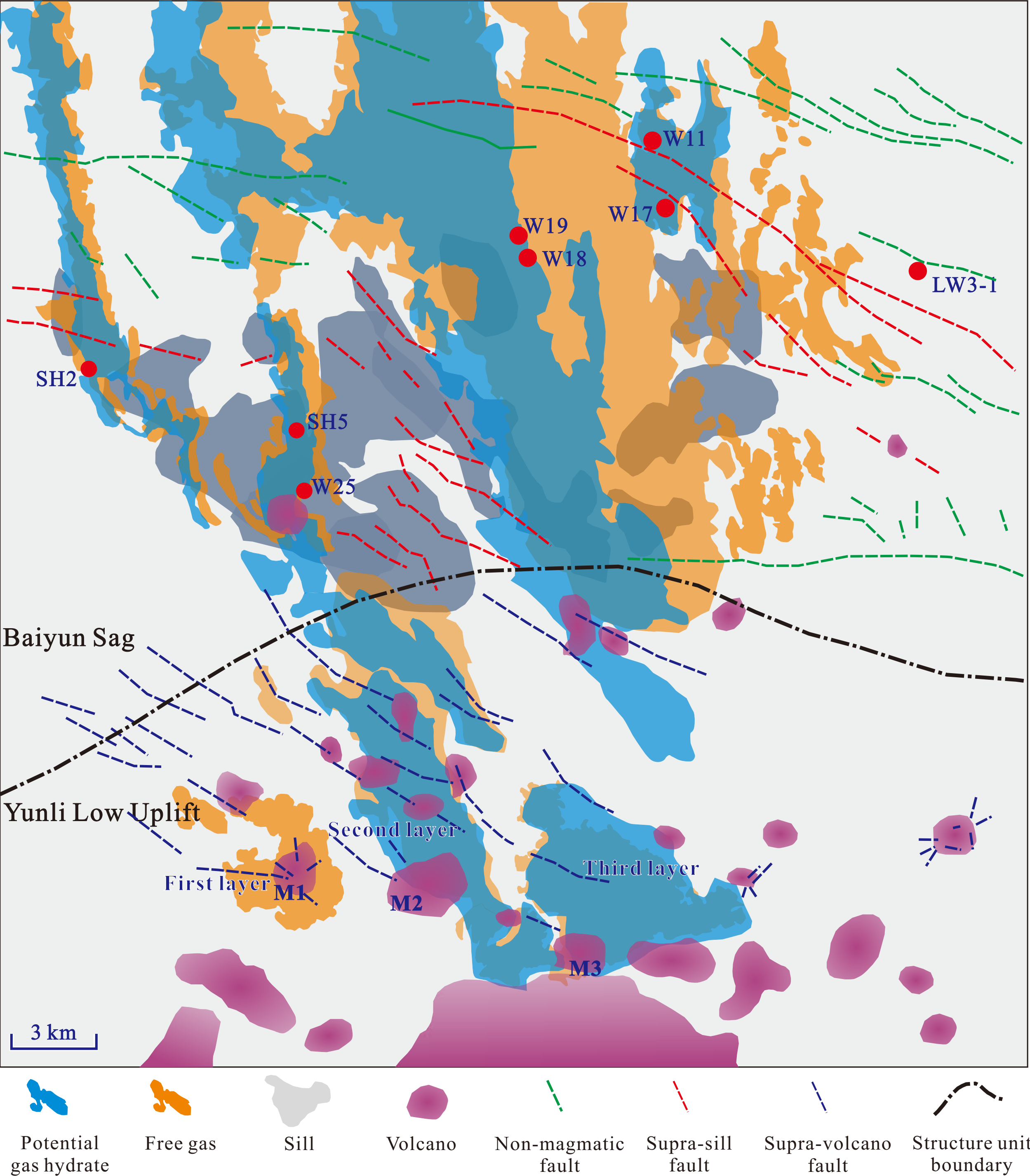
W11
W17
W19
W18
LW3-1
SH2
SH5
W25
Baiyun Sag
Yunli Low Uplift
Second layer
Third layer
First layer
M1
M2
M3
3 km
Potential gas hydrate
Free gas
Sill
Volcano
Non-magmatic fault
Supra-sill fault
Supra-volcano fault
Structure unit boundary

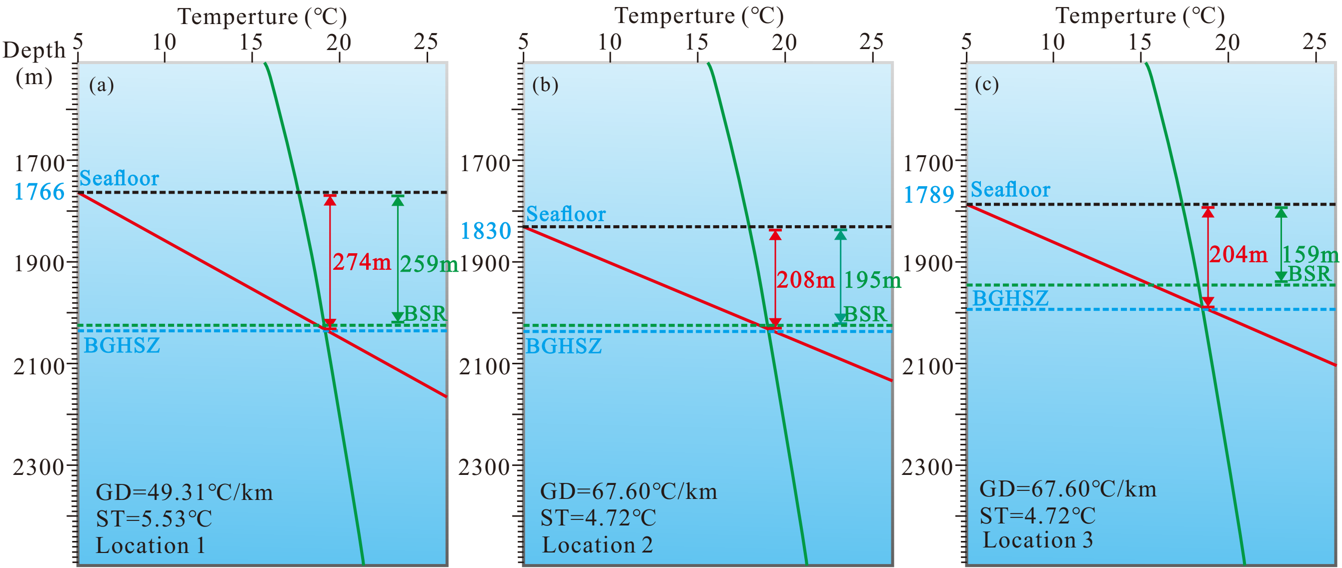Temperture (°C)
Depth (m)
5
10
15
20
25
(a)
1700
Seafloor
1766
274m
259m
BSR
BGHSZ
1900
2100
2300
GD=49.31°C/km
ST=5.53°C
Location 1
(b)
1700
Seafloor
1830
208m
195m
BSR
BGHSZ
1900
2100
2300
GD=67.60°C/km
ST=4.72°C
Location 2
(c)
1700
1789
Seafloor
204m
159m
BSR
BGHSZ
1900
2100
2300
GD=67.60°C/km
ST=4.72°C
Location 3

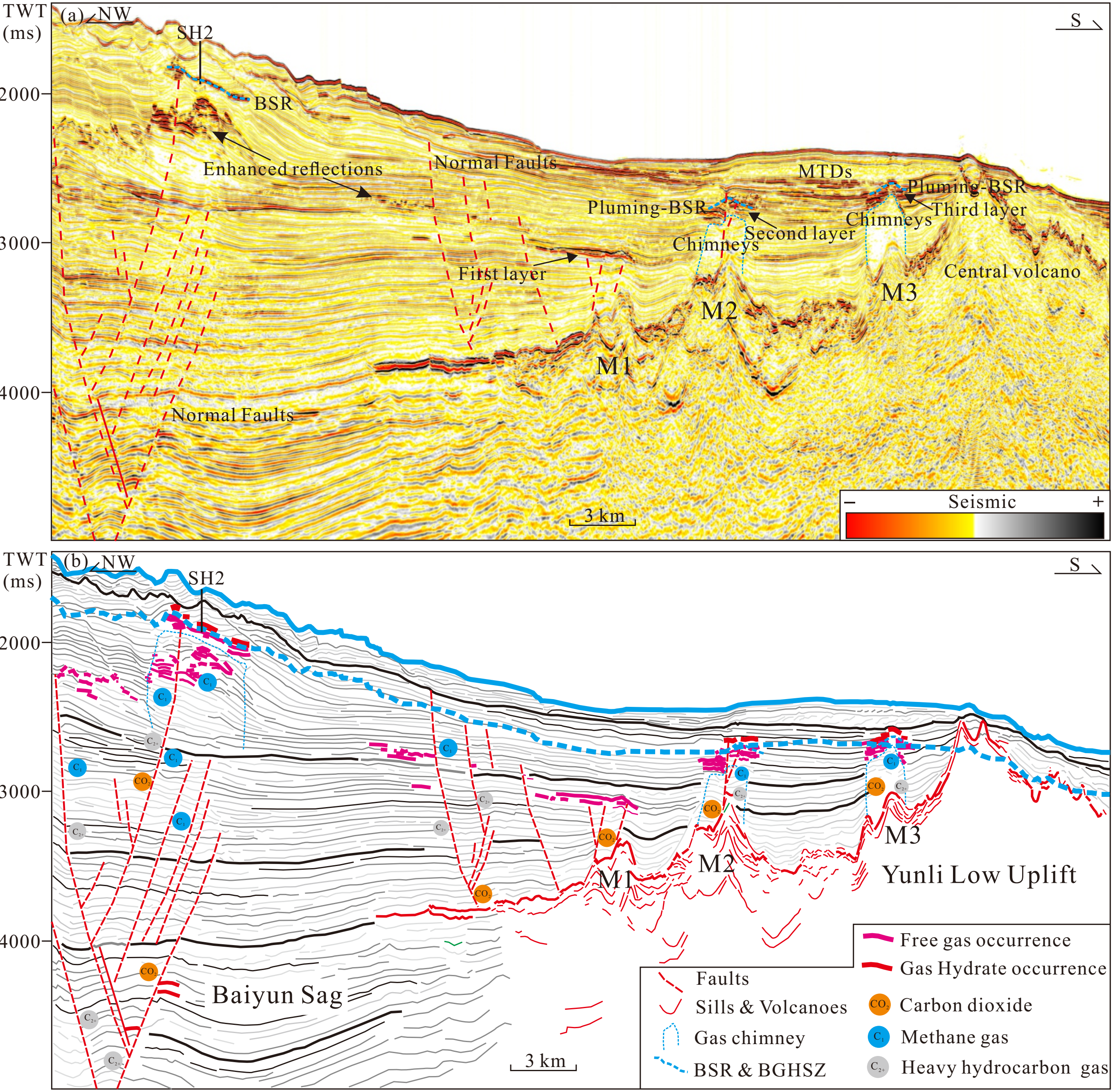
(a)
NW
S
TWT (ms)
2000
3000
4000
SH2
BSR
Enhanced reflections
Normal Faults
MTDs
Pluming-BSR
Second layer
Chimneys
Pluming-BSR
Third layer
Chimneys
First layer
Central volcano
M1
M2
M3
Normal Faults
3 km
Seismic
–
+
(b)
NW
S
TWT (ms)
2000
3000
4000
SH2
M1
M2
M3
Yunli Low Uplift
Baiyun Sag
3 km
Free gas occurrence
Gas Hydrate occurrence
Faults
Sills & Volcanoes
Gas chimney
BSR & BGHSZ
Carbon dioxide
Methane gas
Heavy hydrocarbon gas
CO_2
C_1
C_{2+}